EUROPEAN ORGANIZATION FOR NUCLEAR RESEARCH

MEASUREMENT OF TWO-PARTICLE SEMI-INCLUSIVE RAPIDITY DISTRIBUTIONS AT THE CERN ISR

S.R. Amendolia, G. Bellettini*), L. Bosisio, P.L. Braccini, C. Bradaschia**), R. Castaldi***), V. Cavasinni, C. Cerri, T. Del Prete, L. Foà, P. Giromini**), P. Laurelli, A. Menzione, L. Ristori, G. Sanguinetti and M. Valdata

Istituto Nazionale di Fisica Nucleare, Sezione di Pisa
Istituto di Fisica dell'Università, Pisa
Scuola Normale Superiore, Pisa, Italy.

G. Finocchiaro*), P. Grannis, D. Green†), H. Jöstlein, R. Kephart and R. Thun††)

State University of New York, Stony Brook, New York, USA.

ABSTRACT

We present data on the semi-inclusive distributions of rapidities of secondary particles produced in pp collisions at very high energies. Our experiment was performed at the CERN Intersecting Storage Rings (ISR). The data given here, at centre-of-mass energies of $\sqrt{s}$ = 23 and 62 GeV, include the single-particle distributions and two-particle correlations at fixed charged multiplicity n, as well as the inclusive two-particle correlations. The semi-inclusive correlations show pronounced short-range correlation effects which have a width considerably narrower than in the case of inclusive correlations. We show that these short-range effects can be understood empirically in terms of three parameters whose energy and multiplicity dependence are studied. The data support the picture of multiparticle production in which clusters of small multiplicity and small dispersion are emitted with subsequent decay into hadrons.

Geneva - 19 June 1975

(Submitted to Nuovo Cimento)

---

*) Also at Laboratori Nazionali del CNEN, Frascati, Italy.

**) Present address: DESY, Hamburg, Germany.

***) Present address: CERN, Geneva, Switzerland.

†) Present address: Carnegie-Mellon University, Pittsburgh, Pennsylvania, USA.

††) Present address: University of Michigan, Ann Arbor, Michigan, USA.

1. INTRODUCTION

In the past two years, many experiments[1)] and theoretical analyses[2)] have been performed which sought understanding of the dynamics of multiparticle production in high-energy collisions through data on inclusive distributions. It was realized from the beginning that measurements of single-particle inclusive distributions alone were insufficient to understand details of the production mechanisms. Correlations in phase space among the particles produced in a high-energy collision were expected. Experimental studies have verified the existence of such inclusive correlations between charged particles[3-5)] and between photons and charged particles[6)]. These data show an important positive short-range correlation among secondaries of the pp collisions. The lack of any strong s-dependence of the correlation in the central region is a remarkable fact that might have consequences in the phenomenology of high-energy reactions. However, straightforward interpretation of the data is made difficult by the presence of a long-range component in the rapidity correlations[3)]. It is widely understood that the simultaneous presence of distinct production mechanisms (e.g. diffractive and non-diffractive) can produce such long-range effects; experimental observation of diffractive events at the highest energies[1a,7,8)] indicates that this phenomenon does indeed exist[9)].

The existence of long-range correlations due to interplay of diffractive and non-diffractive mechanisms is, however, only a simple example of a more general property. If high-energy particle production proceeds through a set of separate channels giving rise to different single-particle distributions, then the correlation function, as defined in the following, will contain terms due to the difference in their rapidity distributions. In particular, the differences in single-particle distributions for different values of total charged multiplicities will generate such effects. Thus elucidation of true dynamical correlations is facilitated by a study of the two-charged particle correlations in events with a *fixed* charged multiplicity n (semi-inclusive correlations). Such data have been presented from FNAL measurements[4,10)]. Preliminary data from the Pisa-Stony Brook Collaboration at the CERN ISR have also been reported[1a,8)].

In this paper, we present data on the semi-inclusive single-particle distributions and the semi-inclusive two-particle correlations. These data have been obtained at the CERN ISR for collisions between protons at centre-of-mass energies $\sqrt{s}$ = 23 and 62 GeV. The paper is organized as follows: Section 2 defines the various distribution functions and kinematic variables, Section 3 presents the experimental method and apparatus, and Section 4 discusses the analysis of the data and the various corrections which have been applied. We present our results in Section 5, and conclude in Section 6 with a discussion of the data. In particular,

we show that the semi-inclusive correlations can be understood in terms of a short-range component of universal width and whose amplitude, if expressed in terms of $n/\langle n\rangle$, is also essentially energy-independent. We also show that the data are consistent with a simple and fairly general clustering property among the secondaries produced in pp collisions.

2. KINEMATICS AND OBSERVABLES

In this section we collect together the various definitions and relations among the differential distributions of particles produced in multiparticle reactions, together with some kinematic definitions used in this paper.

We define the single-particle inclusive density

$$\rho^{(1)}(y) = \frac{1}{\sigma}\frac{d\sigma}{dy} , \tag{1}$$

and the two-particle inclusive density

$$\rho^{(2)}(y_1,y_2) = \frac{1}{\sigma}\frac{d^2\sigma}{dy_1 dy_2} , \tag{2}$$

where σ is the total inelastic proton-proton cross-section and y is the rapidity, $y = \sinh^{-1}(p_L/\sqrt{p_T^2 + m^2})$, of an observed secondary particle of mass m and longitudinal and transverse momentum components (p_L,p_T). The invariant cross-sections in (1) and (2) have been integrated over transverse momenta. The two-particle inclusive correlation function is defined:

$$C(y_1,y_2) = \rho^{(2)}(y_1,y_2) - \rho^{(1)}(y_1)\rho^{(1)}(y_2) . \tag{3}$$

In most of the previous experiments, a normalized correlation R has been presented in order to minimize the effect of the uncertainty of the detector efficiencies which are needed to obtain the absolute densities $\rho^{(1)},\rho^{(2)}$ from the experimental rates:

$$R(y_1,y_2) = \frac{\rho^{(2)}(y_1,y_2) - \rho^{(1)}(y_1)\rho^{(1)}(y_2)}{\rho^{(1)}(y_1)\rho^{(1)}(y_2)} . \tag{4}$$

In the present work we have developed reliable means for estimating the corrections to $\rho^{(1)}$ and $\rho^{(2)}$ and thus prefer to present the correlation defined by Eq. (3).

For the semi-inclusive data, we define analogous quantities, making use of the topological inelastic cross-sections σ_n for a fixed number n of charged particles. The semi-inclusive densities become

$$\rho_n^{(1)}(y) = \frac{1}{\sigma_n}\frac{d\sigma_n}{dy} \tag{5}$$

and

$$\rho_n^{(2)}(y_1,y_2) = \frac{1}{\sigma_n}\frac{d^2\sigma_n}{dy_1dy_2} \ . \tag{6}$$

The semi-inclusive quantities are related to inclusive counterparts through

$$\begin{aligned} \sum_n \sigma_n &= \sigma \\ \sum_n \sigma_n\rho_n^{(1)}(y) &= \sigma\rho^{(1)}(y) \\ \sum_n \sigma_n\rho_n^{(2)}(y_1,y_2) &= \sigma\rho^{(2)}(y_1,y_2) \ . \end{aligned} \tag{7}$$

The semi-inclusive correlation is then

$$C_n(y_1,y_2) = \rho_n^{(2)}(y_1,y_2) - \rho_n^{(1)}(y_1)\rho_n^{(1)}(y_2) \ . \tag{8}$$

The relationship between the inclusive and semi-inclusive correlations can be derived to be (see, for instance, Ref. 2c)

$$C(y_1,y_2) = \sum_n \alpha_n C_n(y_1,y_2) + \sum_n \alpha_n\left[\rho^{(1)}(y_1) - \rho_n^{(1)}(y_1)\right]\left[\rho^{(1)}(y_2) - \rho_n^{(1)}(y_2)\right] \ , \tag{9}$$

where $\alpha_n = \sigma_n/\sigma$. This equation demonstrates the assertion made in the first section that the inclusive correlation contains a "crossed term" part, due only to differences in single-particle semi-inclusive distributions, which is non-zero even in the absence of "true" correlations among two charged particles. True dynamical correlations can only be present in the first term in Eq. (9), which is the one containing two-particle densities, and is accessible only through measurement of semi-inclusive distributions. In the present experiment, we obtain directly all the quantities entering into (9) and thus determine the relative importance of the true correlation term and the crossed term.

The normalization properties of the distributions are of importance in our analysis. It is well known that

$$\iint C(y_1,y_2)dy_1dy_2 = \langle n(n-1)\rangle - \langle n\rangle^2 \equiv f_2 \ . \tag{10}$$

Similarly, the semi-inclusive correlation has normalization

$$\iint C_n(y_1,y_2)dy_1dy_2 = -n \ , \tag{11}$$

and at fixed values of y_1,

$$\int C_n(y_1,y_2)dy_2 = -\rho_n^{(1)}(y_1) \ . \tag{12}$$

We note that the integrals of the semi-inclusive correlation are negative quantities.

Finally, we introduce the approximate rapidity variable $\eta = -\ln\left[\tan\left(\theta_{cm}/2\right)\right]$ appropriate to our experiment in which angles, but not momenta or masses, are determined. The variable η is equivalent to y if $(p_T^2/m^2) \gg 1$.

3. EXPERIMENTAL PROCEDURE

The experimental apparatus employed in this work is essentially that used in the measurement of the total proton-proton cross-section, and has been described in detail elsewhere[11]. It consisted of scintillator hodoscopes around each of the ISR beams downstream from the interaction point, as shown in Fig. 1. There was in addition a hodoscope L covering the wide-angle region around the interaction point. Each of the downstream arms consisted of eight hodoscopes, whose structure is illustrated in Fig. 2. Hodoscopes H_1, H_2, H_3, H_4, TB_1, and TB_2 participated in forming the trigger. $H_2\theta$ and $H_4\theta$ were subdivided in narrow bands of polar angle and into azimuthal quadrants or octants as shown. The hodoscope L surrounding the intersection at large angles was similarly subdivided into seven polar bands and azimuthal quadrants as shown in Fig. 2. Counts in these scintillators form the basis for our η-distributions.

The combined hodoscope system covers most of the full solid angle, the major gaps occurring in the range $1.0 < |\eta| < 1.3$. The trigger employed was

$$\{(H_1 \cdot H_2) + (H_3 \cdot H_4) + (TB_1 \cdot TB_2)\}_{left} \cdot \{(H_1 \cdot H_2) + (H_3 \cdot H_4) + (TB_1 \cdot TB_2)\}_{right} .$$

This trigger was sensitive to about 97% of all inelastic events.

Rejection of background, due primarily to interactions of single beams with residual gas or with beam pipes, was made through analysis of time-of-flight differences between different pairs of hodoscopes[11]. In the present work, we have required the observed times-of-flight to be well within the window for beam-beam events. Events in the tails of the time distributions were eliminated so as to reduce background contamination. Using runs with only one circulating beam, we have checked that single-beam backgrounds have negligible effect on our results. We have also determined from experimental studies that random counts in the hodoscopes have negligible effect on our data.

The analysis of the data presented here is based on approximately 10^6 inelastic events at the lowest and highest ISR energies, $\sqrt{s}$ = 23 and 62 GeV. Thus statistical errors are small for single-particle distributions and are also small for correlations in most regions of the phase space. The primary source of error is systematic.

Sources of systematic error derive primarily from the finite resolution of the counters, from the production of secondary particles in interactions with

material surrounding the interaction region, and from strange particle decays. The finite size of the hodoscope counters causes a loss of rate if more than one particle strikes the same element. Secondary particle production may proceed through photon conversion in the vacuum pipe or hodoscope material, hadronic showers in the same material initiated by primary collision products, or by electrons knocked out by charged particles. These secondary processes increase the number of observed particles. They also affect the distributions in that the number and angular distribution of secondaries depend on the primary particle type and momentum as well as on the detailed structure of the material present in the vacuum pipes and hodoscopes. Showers of secondary charged particles (hadronic and electromagnetic) give clusters correlated in space which affect the two-particle distribution. The decays of neutral strange hadrons also tend to increase the observed multiplicity. The combined effect of resolution, secondary production, decays, and missing solid angle is to increase the mean observed charged multiplicity by about 20% over the true value[12] at $\sqrt{s}$ = 23 GeV.

Observation of a count in a hodoscope element requires a minimum momentum of about 80 MeV/c. The measured rate in any element is thus the integral over absolute momentum above this threshold for fixed θ. The loss of particles below the momentum cut-off is negligible. Owing to the centre-of-mass motion in the ISR lab. frame, there are small changes in c.m. angle within the annular rings of H_4 and H_2. The same effect occurs for L, augmented by the fact that its elements are not annular rings. In all results presented here, we use the value of centre-of-mass rapidity η averaged over the ring, obtained through a Monte Carlo calculation. The resulting values of η for each ring of counters are given in Table 1.

4. DATA ANALYSIS AND CORRECTIONS

In our experiment the dominant uncertainties are systematic and depend on the corrections which we apply to our data. Thus we discuss our analysis procedures at some length in this section.

The experimental definitions of the inclusive particle densities defined in (1) and (2) are

$$\rho^{(1)}(\eta) = \frac{1}{N_I} \frac{N^{(1)}(\eta)}{\varepsilon(\eta)} \tag{13}$$

and

$$\rho^{(2)}(\eta_1,\eta_2) = \frac{1}{N_I} \frac{N^{(2)}(\eta_1,\eta_2)}{\varepsilon(\eta_1)\varepsilon(\eta_2)} \, . \tag{14}$$

N_I is the total number of inelastic events contained in the sample; $N^{(1)}(\eta)$ is the number of charged particles detected by the counter ring positioned at η for these events; $N^{(2)}(\eta_1,\eta_2)$ is the corresponding number of coincidences of charged particles in the rings at η_1 and η_2; and $\varepsilon(\eta)$ is the efficiency for counting in the ring at η [13].

The number N_I of inelastic events is obtained from the full sample of events after time-of-flight cuts by subtracting events which correspond to elastic scattering. Elastic events are recognized by their topological properties in the sample; in principle, they are collinear two-prong events. In order to eliminate elastic events in which one or both protons interact in the beam pipes, we use the criterion that any event giving charged particles only at $\theta < 75$ mrad (inside the central hole of H_1) is classified as elastic. The events identified by this cut satisfy the known cross-sections and shape for elastic pp scattering[14-16], but also include a small fraction of inelastic events. We estimate that at $\sqrt{s}$ = 23 GeV, the elastic requirement includes $\approx$ 0.5 mb of the inelastic cross-section, while at $\sqrt{s}$ = 62 GeV we estimate $\approx$ 0.9 mb. In addition, some good inelastic events were lost by the rather restrictive time-of-flight cuts imposed to minimize background. We have checked that our results are insensitive to precise location of these cuts. The final sample of inelastic events corresponds to 30.0 mb at $\sqrt{s}$ = 23 GeV (out of 32.5 mb) and to 32.9 mb at $\sqrt{s}$ = 62 GeV (out of 35.5 mb). The primary loss of inelastic cross-section occurs for the lowest multiplicities, owing to the elastic event definition, which includes some diffractive-like events, and to the trigger requirement of at least one particle into the left and right arms of the hodoscopes, which fails when all particles in one cone are contained in the downstream pipe. For multiplicities greater than half the mean we expect no loss of events in the semi-inclusive distributions.

The counts $N^{(1)}(\eta)$ are obtained for the full azimuthal ring of counters at fixed polar angle. Similarly the counts $N^{(2)}(\eta_1,\eta_2)$ are summed over the various azimuths of counters in the rings at η_1 and η_2; one exception to this azimuthal sum is discussed below in connection with the analysis of the correlation function. We have assumed that azimuthal correlations in inclusive or semi-inclusive distributions are weak[3,6,17,18].

The efficiencies ε in (13) and (14) take into account the geometrical acceptance and also the effects of secondary particle production, decay, and finite counter size. They can be interpreted as the effective width in rapidity of the various counter rings. These efficiencies are computed in a Monte Carlo program which incorporates as nearly as possible all the features of the apparatus and the known particle distributions. The major contribution to the systematic error on our results comes from uncertainty of their evaluation. Details of these calculations are summarized below.

Analogous experimental definitions to (13) and (14) are used for the semi-inclusive densities (5) and (6):

$$\rho_n^{(1)}(\eta) = \frac{1}{N_n} \frac{N_n^{(1)}(\eta)}{\varepsilon_n(\eta)} , \tag{15}$$

$$\rho_n^{(2)}(\eta_1,\eta_2) = \frac{1}{N_n} \frac{N_n^{(2)}(\eta_1,\eta_2)}{\varepsilon_n(\eta_1)\varepsilon_n(\eta_2)} , \tag{16}$$

In these expressions, the subscript n refers to the total *observed* charged multiplicity in the event.

We turn now to a brief description of the Monte Carlo calculation used to determine the efficiencies. The primary inputs to the calculation were the single particle angular distributions measured at the ISR[19] and FNAL[20] and the data on multiplicity distributions[21]. The n-dependence of $\rho_n^{(1)}$ was included on the basis of our raw data and those of FNAL[4], but no dynamical correlations were taken into account. Calculations were also made for studying the sensitivity of our efficiencies to the input distributions using modified multiperipheral models[22] and a nova model[23]. The detailed geometry of the experiment, as well as the irregular vacuum pipe of the ISR and the support structures of the hodoscopes, was included.

A careful attempt was made to account for all possible sources of gain and loss of particles from the original number generated in the collision. Extra particles, produced from the decay of K_S^0 and Λ, were simulated according to data from FNAL and ISR[24]. Secondary hadrons, produced when a particle traverses the material of the ISR vacuum pipe or the detector assembly, were generated according to the known features of nucleon-nucleus and meson-nucleus collisions in the appropriate energy range. Gamma conversions in the material around the interaction region produce e^+e^- pairs which can add to the observed number of particles in the hodoscopes. The gamma sources are the primary π^0's and those π^0's produced in secondary hadronic interactions. The generated multiplicity of π^0's is based on high-energy measurements[21c,25]. Delta-rays can be produced whenever a charged particle traverses material. The spectra of these delta-rays are sharply peaked at low electron energy; however, in some circumstances the low-energy electron may strike a counter before being absorbed. It is further possible that a delta-ray, produced in one counter element, may penetrate to a neighbouring element, giving a spurious count. Finally, there is a loss of counts owing to multiple particle hits of a single hodoscope element which tends to decrease the value of the observed multiplicity.

A complete documentation of the Monte Carlo procedures will be presented elsewhere. Here we simply present a summary of the importance of the various

effects mentioned as computed at $\sqrt{s}$ = 23 GeV. Table 2 shows how these effects influence the mean multiplicity for three angular ranges corresponding to the hodoscopes H_4, H_2, and L both separately and added together.

Several important tests of the Monte Carlo calculation have been performed. In Fig. 3a we show the agreement of our raw single particle distribution $\rho^{(1)}(\eta)$ with the distribution obtained by the Monte Carlo calculation incorporating the various mechanisms for gains and losses discussed above. Figure 3b shows the same comparison for the semi-inclusive distribution $\rho_n^{(1)}(\eta)$, with n = 14-16. We conclude that the combination of the input distributions and Monte Carlo simulation of the experiment reproduces our data well. The rise in $\rho^{(1)}(\eta)$ and $\rho_n^{(1)}(\eta)$ from $\eta = 0$ to $|\eta| = 1.5$ is due to the secondary interactions (mainly γ-conversions) in the vacuum pipe (bicone) surrounding the interaction region, and also to the transformation between y and η. Two values of $\rho^{(1)}(\eta)$ appear in the overlap region of H_2 and H_4 between $|\eta| = 2.80$ and $|\eta| = 3.65$. H_4 shows a higher counting rate due to secondary particle production in the vacuum pipe between H_2 and H_4, and in H_2 itself. The fact that we can reproduce this large difference in $\rho^{(1)}(\eta)$ between H_2 and H_4 gives us confidence in the validity of the Monte Carlo calculation. We have disregarded the H_4 data in the region of the overlap for our subsequent analysis.

As seen from Table 2, the effect of our apparatus is to increase the observed multiplicity over the true multiplicity. We have checked that the Monte Carlo calculation can indeed reproduce the observed multiplicity distribution starting with the true distribution at $\sqrt{s}$ = 23 GeV. In Fig. 4 we show the comparison of our uncorrected data with those produced by our Monte Carlo calculation with FNAL data[21] as input.

A set of events corresponding to fixed *observed* multiplicities contains events whose *true* multiplicity spans a considerable interval owing to the competing effects of secondary particle production and particle losses. In Fig. 5 we show the distribution of true multiplicities contributing to a fixed observed value; we note that the average value is displaced and that the dispersion of true multiplicities is rather large. Our semi-inclusive distributions are therefore weighted averages on the true multiplicity.

The primary use of the Monte Carlo in our analysis is the calculation of the efficiencies $\varepsilon(\eta)$ and $\varepsilon_n(\eta)$ appearing in Eqs. (13)-(16). In the absence of the mechanisms discussed above for particle gain and loss, the ε's represent the interval in η spanned by each hodoscope element. The n-dependence of ε_n was found to be small ($\lesssim$ 10% for n between 10 and 30) except for $|\eta| \leq 1$, where the large physical size of the counters causes a larger loss of particles at high multiplicity. At $\eta \simeq 0$ and the highest multiplicity, ε_n differs from ε by about 25%.

The fact that fixed observed multiplicity in our experiment corresponds to a distribution of true multiplicities creates an additional complication in the calculation of the semi-inclusive correlations. The reason is due to the presence of a crossed term similar to that noted in (9). To show this effect explicitly, we denote by α_m^n the probability of an event of *true* multiplicity m to contribute to the sample of fixed *observed* multiplicity n. Then, in analogy with (9), the *observed* semi-inclusive correlation at observed multiplicity n is

$$C_n^{(obs)}(\eta_1,\eta_2) = \sum_m \alpha_m^n C_m(\eta_1,\eta_2) + \\ + \sum_m \alpha_m^n \left\{ \left[\rho_{m_0}^{(1)}(\eta_1) - \rho_m^{(1)}(\eta_1)\right]\left[\rho_{m_0}^{(1)}(\eta_2) - \rho_m^{(1)}(\eta_2)\right] \right\} , \quad (17)$$

where $m_0 = \sum_m \alpha_m^n m$ = average of the true multiplicities contributing to fixed observed n and $\rho_{m_0}^{(1)}(\eta) = \sum_m \alpha_m^n \rho_m^{(1)}(\eta)$. Since $\sum_m \alpha_m^n = 1$, we find

$$C_n^{(obs)}(\eta_1,\eta_2) = C_{m_0}(\eta_1,\eta_2) + \left\{ \left[\sum_m \alpha_m^n \rho_m^{(1)}(\eta_1)\rho_m^{(1)}(\eta_2)\right] - \rho_{m_0}^{(1)}(\eta_1)\rho_{m_0}^{(1)}(\eta_2) \right\} . \quad (18)$$

The second term of (18) represents a correction which must be subtracted from the observed semi-inclusive correlation to obtain the true correlation, denoted in (18) as $C_{m_0}(\eta_1,\eta_2)$. It is $C_{m_0}(\eta_1,\eta_2)$ for which data are presented below; the fact that it is averaged over near-by true multiplicities is found to be of no importance. We have performed this correction to the data using α_m^n from the Monte Carlo calculation and the known dependence of $\rho_n^{(1)}(\eta)$ on n. The sign of the second term is positive for most η_1 and η_2. This can be seen qualitatively for $\eta_1 \approx \eta_2 \approx 0$ since $\rho_n^{(1)}(0) \cong n$ and thus

$$\left[\sum_m \alpha_m^n \rho_m^{(1)}(0)\rho_m^{(1)}(0)\right] > \left[\rho_{m_0}^{(1)}(0)\rho_{m_0}^{(1)}(0)\right] .$$

In the limit that $\alpha_m^n = \delta_{mm_0}$ the correction vanishes.

A final feature of the data analysis must be explained. Examination of the various mechanisms for producing spurious particles via secondary interactions shows several which make showers of secondaries localized in space. We have studied the effect of this spurious clustering by making use of the quadrant structure of our hodoscopes in azimuth. We calculate separately $\rho_n^{(2)}(\eta_1,\eta_2)$ for the cases where particles 1 and 2 fall into the same azimuthal quadrant, adjacent quadrants, or opposite quadrants. This treatment of the data shows similar results for the adjacent and opposite pairings with noticeably larger values for the same quadrant pairs. An effect of the same type and size is predicted by our Monte Carlo calculation as a consequence of secondary interactions. Therefore, although we cannot exclude the existence of a small dynamical contribution, we have removed all this effect by computing $\rho_n^{(2)}(\eta_1,\eta_2)$ excluding all the same quadrant pairs and applying a correction factor. A similar procedure was also followed

in our earlier determination of the inclusive correlations and was discussed elsewhere[3]. This correction factor would be 4/3 in the absence of all azimuthal correlations. In fact there are small azimuthal correlations which favour emission of particles near $\Delta\phi = \pi$ compared with $\Delta\phi = 0$ [3,6,18]. We include this effect by correcting $\rho_n^{(2)}$ by the factor $(4/3)(1 - \Delta)$, where Δ is taken from the azimuthal correlations and is about 0.02. This value of Δ has a non-negligible effect on C_n. Since C_n contains the difference of two similar quantities, $\rho^{(2)}(\eta_1,\eta_2)$ and $\rho^{(1)}(\eta_1)\rho^{(1)}(\eta_2)$, a 2% correction on $\rho^{(2)}(\eta_1,\eta_2)$ implies a variation of the correlation function beyond its intrinsic systematic errors.

We have checked our results for internal consistency. This check, using the sum rule (12), is made to the final data after the correction of the efficiencies for spurious particle gain and loss and the correction to the correlation for the cross-term arising from the spread in true multiplicities contributing to fixed observed multiplicities shown in (18). The sum rule is well satisfied and indicates that our handling of the rightmost term in (18) and the correction for azimuthal correlations are valid. Had we not taken into account these corrections, the sum rule (12) would have been violated by 10-20%.

5. RESULTS

Presentation of data for all the distribution functions discussed above, particularly the semi-inclusive correlation with two rapidity and one multiplicity variables, would require a very large amount of numerical information. In this section we give a sample of our results which we feel to be representative of the data, based on about 7×10^5 inelastic events at each energy.

The normalized inclusive correlations [Eq. (4)] were presented in our earlier publication[3]. As discussed in detail in that paper, these functions show a prominent short-range positive correlation effect. For comparison with the semi-inclusive distributions, we show here the undivided inclusive correlations [Eq. (3)] at both $\sqrt{s}$ = 23 and 62 GeV for $\eta_1 = 0$. These distributions are plotted in Fig. 6 and shown in Tables 3 and 4. At $\sqrt{s}$ = 23 GeV, the correlation is appreciable in magnitude for $|\eta| \lesssim 2$. The width of $C(0,\eta)$ broadens with increasing s, which can be qualitatively understood on the basis of scaling hypotheses[26]. An important feature of the inclusive correlations to be borne in mind for comparison with the semi-inclusive correlations presented below is the rather broad rapidity region in which the correlation is positive and appreciably non-zero.

We turn now to the semi-inclusive distributions. We have chosen to present our results at three fixed charge multiplicities at both values of $\sqrt{s}$. We have chosen to restrict our attention to multiplicities above 10 in order to minimize the effects due to the diffractive component. Figure 7 shows the semi-inclusive single particle density $\rho_n^{(1)}(\eta)$ at three multiplicities and both energies.

Numerical values are given in Table 5. The dip at $\eta = 0$ is due to the y to η transformation; the data are consistent with a y-distribution with a maximum at $y = 0$.

The semi-inclusive correlations are presented for three values of n as a function of η_2, with η_1 fixed at three values. The data at $\sqrt{s} = 23$ GeV are shown in Fig. 8 and Table 6; data at $\sqrt{s} = 62$ GeV are shown in Fig. 9 and Table 7. The most prominent feature of these distributions is the appearance of a sharp positive peak at $\eta_1 \approx \eta_2$, the width of which is considerably smaller than that of the inclusive correlation (Fig. 6). This short-range correlation structure is superimposed on a broad negative curve as is required in order that the sum rule (12) be satisfied. The width of the short-range peak is remarkably independent of both n and $\sqrt{s}$.

We stress here that this conclusion is extremely insensitive to the various corrections applied to the data and discussed in Section 4. All the corrections, including the Monte Carlo calculations of efficiencies, subtraction of the crossed-term in (18), and accounting for the effect of azimuthal correlations, were observed in our analysis to leave the height and width of the short-range peak unchanged. These corrections have merely changed the size of the broad negative curve on which the peak is superimposed.

In this experiment we measure all inclusive and semi-inclusive one- and two-particle densities directly; thus we may assess the relative importance of the two terms in (9). The first term, formed from the weighted sum of semi-inclusive correlations, is shown in Fig. 10 for the two energies. It has a shape almost identical to any of its constituents. The second term, arising from the difference of semi-inclusive single-particle distributions from the inclusive ones, also shown in Fig. 10, is predominantly positive and displays a broad quasi-flat central plateau. The magnitude of the crossed term exceeds the true correlation term magnitude by more than a factor of two. Therefore, the dominant contribution to the observed inclusive correlation function is the crossed term; *the effect of true dynamical correlations are masked in the inclusive measurements*. We note that the shape of the crossed term is similar to the observed $\pi^-\pi^-$ correlation at FNAL[27]. Our crossed term in Fig. 10 is somewhat broader than $C^{--}(0,y)$. This may be qualitatively understood by the fact that our $\rho^{(1)}$ and $\rho_n^{(1)}$ include the proton distributions which are important at $\eta \gtrsim 2$, whereas the distributions entering into $C^{--}(0,y)$ do not. The magnitude of the observed $C^{--}(0,0)$ is in qualitative agreement with that of our crossed term. The similarity of the two sets of data suggests that like charge correlations can indeed be understood as due mainly to the variation of $\rho_n^{(1)}(y)$ with n and that little dynamical correlation need be invoked[28].

Our results can also be compared with previously reported data from the ISR[18] at the lower of our energies. The authors of Ref. 18 use a somewhat different definition of the correlation function, normalized to zero. In terms of the quantities defined in this paper their semi-inclusive correlation is

$$C_n^{II}(\eta_1,\eta_2) = \frac{1}{n(n-1)}\rho_n^{(2)}(\eta_1,\eta_2) - \frac{1}{n^2}\rho_n^{(1)}(\eta_1)\rho_n^{(1)}(\eta_2) \ . \qquad (19)$$

In order to reduce the errors they average over n according to

$$C^{II}(\eta_1 - \eta_2) = \langle (n-1)C_n^{II}(\eta_1,\eta_2)\rangle \ , \qquad (20)$$

where the average is taken over $|\eta| \leq 2$ and $6 \leq n \leq 15$ (n is here the number of charged particles in the region $|\eta| \leq 2$). We have analysed our data to obtain $C^{II}(\eta_1 - \eta_2)$ and present our results at $\sqrt{s}$ = 23 GeV together with those of Ref. 18 in Fig. 11a. We observe again the existence of the short-range correlation peak. Figure 11b shows the behaviour of $C^{II}(\eta_1 - \eta_2)$ at $\sqrt{s}$ = 62 GeV. The data of Fig. 11 represent the projections of the correlation function onto the line $\eta_1 + \eta_2 = 0$. We recall that this line is perpendicular to the contours of constant correlation[3,8] in the central region.

To summarize, the semi-inclusive correlations presented here have rather simple properties. The short-range component, identified by the positive-going peak is present in all samples of the data. The shapes of these peaks are nearly independent of multiplicity and energy. The existence of this short-range component is difficult to infer from inclusive measurements alone. Our data agree well with the low-statistics studies of semi-inclusive charge-charge correlations obtained from bubble-chamber experiments at FNAL[4], and streamer chamber measurements at the ISR[18].

6. DISCUSSION OF THE DATA

We turn now to a phenomenological discussion of our semi-inclusive correlation data in order to extract some physical insight into the mechanism producing the short-range correlation behaviour noted above. It appears natural to view these data in terms of two components which add to give the observed $C_n(\eta_1,\eta_2)$. The first term is a purely short-range correlation, while the second is a smoothly varying negative background term. In order not to confuse the discussion we focus upon the correlation with one argument set to zero: $C_n(0,\eta_2)$. This choice gives a function for which the phase-space constraints are symmetric in η_2.

The positive short-range term is well fitted at all n and $\sqrt{s}$ by a Gaussian function. The negative background function is chosen according to the following recipe. For independent emission at fixed multiplicity one would have

$$\rho_n^{(2)}(0,\eta_2) = \left[\frac{n-1}{n}\,\rho_n^{(1)}(0)\right]\rho_n^{(1)}(\eta_2) \tag{21}$$

implying

$$C_n(0,\eta_2) = -\left[\frac{1}{n}\,\rho_n^{(1)}(0)\right]\rho_n^{(1)}(\eta_2)\ . \tag{22}$$

We choose then, as suggested by (22), to take the background function as proportional to $\rho_n^{(1)}(\eta_2)$. This choice does not have fundamental justification, but appears to work well in fitting our data. Thus the empirical form to be fitted is

$$C_n(0,\eta) = A_n\, e^{-\eta^2/2\delta_n^2} - B_n\,\rho_n^{(1)}(\eta)\ . \tag{23}$$

As observed in Figs. 8 and 9, the shape of the short-range central peak in the correlation is essentially independent of both n and $\sqrt{s}$. We have made a χ-square fit to (23) at each n and $\sqrt{s}$, letting A_n, B_n, and δ_n vary. We find that where δ_n is well determined by the fit, it is constant at 0.85. At the largest and smallest n, δ_n is not well determined, but is consistent with this value. In order to simplify the analysis, we have chosen to fix $\delta_n = 0.85$ and to determine the best values of A_n and B_n in a χ-square fit. The resulting values are shown in Figs. 12 and 13 as a function of the true charged multiplicity. The results for A_n are given in terms of the quantity $\left[A_n/\rho_n^{(1)}(0)\right]$ in order to eliminate the dependence on the density of the first particle. We observe that at both energies $\left[A_n/\rho_n^{(1)}(0)\right]$ and B_n increase with increasing multiplicities: the rate of increase with n is larger at $\sqrt{s}$ = 23 GeV than at $\sqrt{s}$ = 62 GeV. However, it is possible to view the results at the two energies as being essentially the same. This is achieved by displaying $\left[A_n/\rho_n^{(1)}(0)\right]$ and B_n at both energies as a function of the scaled multiplicity variable $n/\langle n\rangle$. This is shown in Figs. 14 and 15, where it is seen that the parameters for the two energies are much more similar to each other when plotted in terms of the scaled multiplicity.

To show the quality of the fits, we define the quantity

$$C_n^*(0,\eta) = C_n(0,\eta) + B_n\,\rho_n^{(1)}(\eta)\ . \tag{24}$$

In Fig. 16 we compare the data for $C_n^*(0,\eta)$ with the values of the fit to the short-range Gaussian term, $A_n\, e^{-\eta^2/2\delta^2}$. We observe that the fit is good ($\chi^2 \leq 60$ for 41 degrees of freedom) in all cases except the lowest n at $\sqrt{s}$ = 23 GeV. For this particular case, our choice of background term was not adequate; the data require a narrower function than $\rho_n^{(1)}(\eta)$. We summarize the data fitting by the statement that our data are well represented by Eq. (23) in which the s-dependence of the parameters $\left[A_n/\rho_n^{(1)}(0)\right]$ and B_n -- if it is there at all -- is quite small, when n is expressed in units of $\langle n\rangle$.

We may compare our results with the predictions of an uncorrelated cluster model for the non-diffractive component of multiparticle production[29,30]. These models should be valid for $n \gtrsim \langle n \rangle$ and suggest that

$$C_n(0,y) = \frac{\langle k(k-1)\rangle}{2\sqrt{\pi}\sigma\langle k\rangle}\,\rho_n^{(1)}(0)\; e^{-y^2/4\sigma^2} - \frac{\rho_n^{(1)}(0)}{n}\,\rho_n^{(1)}(y)\left[1 + \frac{\langle k(k-1)\rangle}{\langle k\rangle}\right]. \tag{25}$$

Here k is the charge multiplicity of the cluster decay and σ is the width of the distribution of the cluster decay products in rapidity. The parameter σ is generally constrained in order to fit the p_T dependence of the invariant distributions by virtue of the assumption of isotropic cluster decay. This assumption leads to a value[31] of σ near 0.6 units of the η-variable and is in good agreement with our result (23) and $\delta = \sqrt{2}\sigma = 0.85$. The similarity of our phenomenological form (23) and the cluster model prediction (25) immediately allows us to determine the value of $\langle k(k-1)\rangle/\langle k\rangle$ from our values of $\left[A_n/\rho_n^{(1)}(0)\right]$ and B_n. In Fig. 17 we show the variation of $\langle k(k-1)\rangle/\langle k\rangle$ found from A_n and B_n. We have found that the evaluation of $\langle k(k-1)\rangle/\langle k\rangle$ from the fitted A_n and B_n gave almost identical results.

The explicit form of the function $\langle k(k-1)\rangle/\langle k\rangle$ versus n can yield further information on the multiplicity distribution within a cluster. If, for example, all clusters were to decay into a fixed number of particles k_0, then $\langle k(k-1)\rangle/\langle k\rangle = k_0 - 1$ and there is no n-dependence. If, on the other hand, the cluster is a Poisson distribution in k, $\left[\langle k(k-1)\rangle/\langle k\rangle\right]_n \approx (n-1)(\langle k\rangle/\langle n\rangle)$ at a fixed multiplicity n [30].

Our results in Fig. 17 show $\langle k(k-1)\rangle/\langle k\rangle$ to be an increasing function of n, though the increase is less than that predicted with the relatively broad Poisson cluster multiplicity distribution. Within the context of simple independent cluster emission models, our results imply that the cluster multiplicity distribution is intermediate between delta function and Poisson -- thus that the cluster multiplicity dispersion is of order 1. However, we should bear in mind that the models leading to this conclusion [embodied in (25)] are most likely naïve simplifications of reality. In particular, we find it plausible that for large multiplicities ($n \sim 2\langle n\rangle$) the clusters themselves may indeed become correlated. For instance, one could envisage that large-n events may consist of several clusters, all of which tend to decay into greater than the average number of particles. Thus we would caution against a literal interpretation of our results in the existing cluster model framework, particularly with regard to the n-dependence of the cluster multiplicity moments.

To summarize, we find that the expectations based on the uncorrelated cluster model conform to our data. The properties of the clusters are essentially independent of $\sqrt{s}$. Using the value of $\langle k(k-1)\rangle/\langle k\rangle$ for the data near $n = \langle n\rangle$ we infer that the mean cluster multiplicity $\langle k\rangle$ is about 2. This conclusion seems relatively independent of the details of the cluster multiplicity distribution and is drawn from the region where the critical assumption of cluster independence should be most valid. A picture in which clusters are produced with mean charge multiplicity of about 2 with a dispersion of order 1 appears to us quite striking in its simplicity. We might imagine that the clusters inferred from these data are just the familiar class of boson resonances as suggested by various authors[18,32]. Indeed, we note that a statistical mixture of ρ, ω, f, A_2 in the final state of pp collisions would result in cluster parameters very like those which we observe.

Acknowledgements

We are greatly indebted to A. Bechini for his assistance during the data-taking phase. We record with gratitude our appreciation to the ISR staff for their unceasing effort in providing excellent running conditions. We have benefited in this work from useful discussions with many physicists, particularly E.L. Berger and W. Ko.

REFERENCES AND FOOTNOTES

1) Recent reviews of inclusive data include
   a) L. Foà, J. Phys. (France) 34, Suppl. 10, C1-317 (1973).
   b) J. Whitmore, Phys. Reports 10C, 273 (1974).
   c) H. Bøggild and T. Ferbel, to be published in Annu. Rev. Nuclear Sci.
   d) W. Ko, *in* Proc. 17th Internat. Conf. on High-Energy Physics, London, 1974 (Rutherford Lab., Chilton, Didcot, 1974), p. I-76.

2) A summary of theoretical models can be found in
   a) K. Zalewski, *in* Proc. 17th Internat. Conf. on High-Energy Physics, London, 1974 (Rutherford Lab., Chilton, Didcot, 1974), p. I-93.
   b) A. Muller, J. Phys. (France) 34, Suppl. 10, C1-307 (1973).
   c) A. Białas, *in* Proc. 4th Internat. Symposium on Multiparticle Hadrodynamics, Pavia, 1973 (INFN, 1974), p. 511.

3) S.R. Amendolia et al., Phys. Letters 48B, 359 (1974).

4) R. Singer et al., Phys. Letters 49B, 481 (1974).

5) C. Bromberg et al., Phys. Rev. D 9, 1864 (1974).

6) H. Dibon et al., Phys. Letters 44B, 313 (1973).

7) M.G. Albrow et al., Phys. Letters 44B, 207 (1973).

8) G. Bellettini, *in* Proc. 5th Internat. Conf. on High-Energy Collisions, Stony Brook, 1973 (ed. C. Quigg) (American Inst. Phys., New York, 1973), p. 9.

9) A summary of models relating explicitly to correlations is given by A. Białas, Ref. 2c.

10) C. Bromberg et al., paper submitted to 17th Internat. Conf. on High-Energy Physics, London, 1974.

11) a) S.R. Amendolia et al., Nuovo Cimento 17A, 735 (1973).
    b) S.R. Amendolia et al., *in* Proc. 5th Internat. Conf. on Instrumentation for High-Energy Physics, Frascati, 1973 (CNEN, Frascati, 1973), p. 39.

12) F.T. Dao et al., Phys. Rev. Letters 29, 1627 (1972).

13) We have approximated the efficiency for the two-particle density; $\varepsilon^{(2)}(\eta_1,\eta_2) \simeq \varepsilon(\eta_1)\varepsilon(\eta_2)$ in Eq. (14). The effect of correlations in the efficiencies themselves is small and has been taken into account together with the effect of azimuthal correlations at the end of Section 4.

14) U. Amaldi et al., Phys. Letters 44B, 112 (1973).

15) G. Barbiellini et al., Phys. Letters 39B, 663 (1972).

16) V.D. Bartenev, Phys. Rev. Letters 31, 1088 (1973).

17) Detailed studies of azimuthal correlations are made for γ-charged coincidences as a function of $p_T(\gamma)$ by G. Finocchiaro et al., Phys. Letters 50B, 396 (1974). The data show that for $p_T(\gamma) < 1.5$ GeV/c the correlations are weak.

18) K. Eggert et al., Angular correlations between charged particles in pp collisions at ISR energies, Nuclear Phys. B86, 201 (1975).

19) a) A. Bertin et al., Phys. Letters, 38B, 260 (1972).
b) M. Banner et al., Phys. Letters, 41B, 547 (1972).
c) M.G. Albrow et al., Nuclear Phys. B54, 6 (1973).

20) The NAL data on inclusive distributions are summarized by J. Whitmore, Ref. 1b.

21) a) C. Bromberg et al., Phys. Rev. Letters 31, 1563 (1973).
b) S. Barish et al., Phys. Rev. D 9, 2688 (1974).
c) F.T. Dao et al., Phys. Rev. Letters 29, 1686 (1972).

22) We are indebted to Dr. C. Risk for providing us with computer generated events using a multiperipheral approach.

23) We appreciate the assistance of Dr. J. Kasman in providing Monte Carlo events based on a nova model.

24) a) M. Antinucci et al., Nuovo Cimento Letters 6, 121 (1973).
b) F.T. Dao et al., Phys. Rev. Letters 30, 1151 (1973).
c) G. Charlton et al., Phys. Rev. Letters 30, 574 (1973).

25) a) G. Neuhofer et al., Phys. Letters 38B, 51 (1972).
b) G. Charlton et al., Phys. Rev. Letters 30, 1192 (1973).

26) This point has been dealt with in more detail in Ref. 3 in which the correlation is studied in the fragmentation region as a function of a projectile rapidity variable.

27) Iowa State-Maryland-Michigan State-FNAL-ANL Collaboration paper presented at the Berkeley Meeting of the APS/DPF, 1973. Also contributed paper (167) by the ANL-Iowa State-Maryland-Michigan State-FNAL Collaboration at the 17th Internat. Conf. on High-Energy Physics, London, 1974.

28) A similar conclusion has been reached by W. Ko in Ref. 1d on the basis of semi-inclusive $\pi^-\pi^-$ correlations at FNAL and Serpukhov.

29) Many authors have discussed cluster models for particle production beginning with G. Cocconi, Phys. Rev. 111, 1699 (1958). Recent reviews and lists of references can be found in A. Białas, Ref. 2c, and G. Ranft and J. Ranft, Nuclear Phys. B83, 285 (1974).

30) E.L. Berger, Nuclear Phys. B85, 61 (1975).

31) The value of σ obtained in independent cluster models with isotropic decays of the clusters is $\sigma \approx 0.9$. This result is based upon fitting zero mass particles to the observed p_T distribution. When the masses of the hadrons are considered, the prediction for σ decreases to $0.4 < \sigma < 0.7$, depending on the mass. See A. Białas, M. Jacob and S. Pokorski, Nuclear Phys. B75, 259 (1974).

32) F. Hayot, Nuovo Cimento Letters 12, 676 (1975).
C. Quigg, P. Pirilä and G. Thomas, Phys. Rev. Letters 34, 290 (1975).

Table 1

Positions of the counter rings

Counter No.	$\langle \eta \rangle$
L4	0.00
L3	0.32
L2	0.61
L1	0.87
$H_2$10	1.35
$H_2$9	1.47
$H_2$8	1.61
$H_2$7	1.77
$H_2$6	1.96
$H_2$5	2.20
$H_2$4	2.47
$H_2$3	2.80
$H_2$2	3.21
$H_2$1	3.65
$H_4$8	3.96
$H_4$7	4.13
$H_4$6	4.29
$H_4$5	4.42
$H_4$4	4.53
$H_4$3	4.67
$H_4$2	4.82
$H_4$1	4.99

Table 2

Summary of the effects giving an increase in the number of observed particles at $\sqrt{s}$ = 23 GeV. These numbers are calculated, through the Monte Carlo program discussed in the text, separately for the hodoscope arrays L, H_2, H_4 and for them altogether. We quote the fractional change in $\langle n_{ch} \rangle$ observed in each hodoscope; each effect is already affected by the finite size of counters, which tends to lower any single mechanism's contribution. Typical statistical errors are ±2% in L, ±1% in H_2, ±5% in H_4, and ±1% for L + H_2 + H_4

Effect	$\frac{\Delta\langle n \rangle}{\langle n \rangle}$ (H_4)	$\frac{\Delta\langle n \rangle}{\langle n \rangle}$ (H_2)	$\frac{\Delta\langle n \rangle}{\langle n \rangle}$ (L)	$\frac{\Delta\langle n \rangle}{\langle n \rangle}$ All hodos.
1. γ-conversion in vacuum pipe or hodoscopes	0.16	0.31	0.11	0.23
2. Strange particle decay	0.05	0.17	0.13	0.15
3. Baryon showers	0.09	0.09	0.03	0.06
4. Meson showers	0.04	0.07	0.05	0.06
5. δ-rays	0.05	0.10	0.06	0.08
All effects together [a]	0.33	0.56	0.34	0.45 [b]

a) All the effects together give a contribution lower than the sum of the single mechanisms: this happens because more than one mechanism can contribute to fire the same counter inside the same event.

b) This figure corresponds to a 0.2 fractional change on the full solid angle due to the incomplete angular coverage of the apparatus.

Table 3

Inclusive correlation function $C(\eta_1,\eta_2)$ at $\eta_1 = 0$ and $\sqrt{s} = 23$ GeV versus η_2. Errors are statistical. The data have been symmetrized around $\eta = 0$.

η_2	$C(0,\eta_2)$
0.00	1.692 ± 0.009
0.32	1.678 ± 0.009
0.61	1.561 ± 0.010
0.87	1.423 ± 0.010
1.35	1.039 ± 0.012
1.47	0.896 ± 0.010
1.61	0.752 ± 0.009
1.77	0.594 ± 0.008
1.96	0.477 ± 0.007
2.20	0.305 ± 0.006
2.47	0.137 ± 0.005
2.80	0.035 ± 0.004
3.21	-0.045 ± 0.003
3.65	-0.095 ± 0.002
3.96	-0.099 ± 0.003
4.13	-0.099 ± 0.003
4.29	-0.089 ± 0.003
4.42	-0.089 ± 0.003
4.53	-0.078 ± 0.003
4.67	-0.073 ± 0.002
4.82	-0.051 ± 0.002
4.99	-0.042 ± 0.002

Table 4

Inclusive correlation function $C(\eta_1,\eta_2)$ at $\eta_1 = 0$ and $\sqrt{s} = 62$ GeV versus η_2. Errors are statistical. The data have been symmetrized around $\eta = 0$.

η_2	$C(0,\eta_2)$
0.00	2.231 ± 0.010
0.32	2.209 ± 0.010
0.61	2.121 ± 0.011
0.87	2.039 ± 0.011
1.35	1.632 ± 0.013
1.47	1.479 ± 0.012
1.61	1.378 ± 0.011
1.77	1.221 ± 0.010
1.96	1.101 ± 0.009
2.20	0.917 ± 0.008
2.47	0.700 ± 0.007
2.80	0.464 ± 0.006
3.21	0.210 ± 0.005
3.65	0.014 ± 0.004
3.96	-0.056 ± 0.005
4.13	-0.072 ± 0.005
4.29	-0.083 ± 0.005
4.42	-0.083 ± 0.005
4.53	-0.086 ± 0.004
4.67	-0.092 ± 0.004
4.82	-0.105 ± 0.003
4.99	-0.100 ± 0.003

Table 5

Semi-inclusive single-particle density, $\rho_\eta^{(1)}(\eta)$, versus η. n_{obs} is the observed multiplicity and n_{true} is the corresponding mean true charged multiplicity. Errors are systematic and reflect the uncertainty in the efficiency corrections. The data have been symmetrized around $\eta = 0$.

	$\sqrt{s}$ = 23 GeV			$\sqrt{s}$ = 62 GeV		
η	n_{obs} = 10, 11 (n_{true} = 9.1)	n_{obs} = 14, 15 (n_{true} = 14.0)	n_{obs} = 20, 21 (n_{true} = 21.7)	n_{obs} = 10, 11 (n_{true} = 8.1)	n_{obs} = 20, 21 (n_{true} = 18.8)	n_{obs} = 30, 31 (n_{true} = 30.8)
0.00	1.54 ± 0.05	2.63 ± 0.09	4.60 ± 0.11	0.92 ± 0.05	2.67 ± 0.07	4.87 ± 0.10
0.32	1.56 ± 0.05	2.72 ± 0.09	4.71 ± 0.12	0.99 ± 0.06	2.77 ± 0.10	4.98 ± 0.14
0.61	1.64 ± 0.05	2.81 ± 0.10	4.85 ± 0.14	1.05 ± 0.07	2.91 ± 0.11	5.23 ± 0.16
0.87	1.65 ± 0.07	2.84 ± 0.11	4.94 ± 0.15	1.11 ± 0.07	3.05 ± 0.11	5.60 ± 0.19
1.35	1.55 ± 0.14	2.72 ± 0.23	4.43 ± 0.34	1.10 ± 0.14	3.03 ± 0.27	5.57 ± 0.41
1.47	1.41 ± 0.13	2.46 ± 0.21	4.13 ± 0.29	1.06 ± 0.14	2.85 ± 0.24	5.08 ± 0.36
1.61	1.34 ± 0.10	2.27 ± 0.17	3.61 ± 0.24	1.00 ± 0.13	2.70 ± 0.22	4.68 ± 0.31
1.77	1.24 ± 0.09	2.03 ± 0.14	3.11 ± 0.18	0.97 ± 0.11	2.59 ± 0.17	4.43 ± 0.22
1.96	1.20 ± 0.07	1.87 ± 0.09	2.80 ± 0.13	0.95 ± 0.09	2.50 ± 0.13	4.06 ± 0.15
2.20	1.11 ± 0.05	1.62 ± 0.08	2.14 ± 0.11	0.95 ± 0.08	2.36 ± 0.10	3.41 ± 0.13
2.47	0.98 ± 0.05	1.32 ± 0.07	1.54 ± 0.09	0.92 ± 0.08	2.15 ± 0.10	3.01 ± 0.12
2.80	0.77 ± 0.03	0.96 ± 0.05	1.05 ± 0.05	0.87 ± 0.06	1.85 ± 0.09	2.44 ± 0.11
3.21	0.60 ± 0.03	0.61 ± 0.03	0.59 ± 0.04	0.78 ± 0.05	1.42 ± 0.08	1.70 ± 0.08
3.65	0.34 ± 0.03	0.30 ± 0.03	0.25 ± 0.03	0.63 ± 0.05	0.92 ± 0.08	0.84 ± 0.07
3.96	0.29 ± 0.02	0.22 ± 0.01	0.20 ± 0.01	0.59 ± 0.03	0.73 ± 0.04	0.66 ± 0.03
4.13	0.22 ± 0.01	0.15 ± 0.01	0.14 ± 0.01	0.55 ± 0.03	0.65 ± 0.03	0.59 ± 0.03
4.29	0.17 ± 0.01	0.13 ± 0.01	0.11 ± 0.01	0.47 ± 0.02	0.54 ± 0.03	0.49 ± 0.02
4.42	0.14 ± 0.01	0.10 ± 0.01	0.08 ± 0.01	0.44 ± 0.02	0.46 ± 0.02	0.41 ± 0.02
4.53	0.13 ± 0.01	0.10 ± 0.01	0.07 ± 0.01	0.34 ± 0.02	0.42 ± 0.02	0.32 ± 0.02
4.67	0.10 ± 0.01	0.08 ± 0.01	0.05 ± 0.01	0.33 ± 0.02	0.34 ± 0.02	0.27 ± 0.01
4.82	0.09 ± 0.01	0.05 ± 0.01	0.02 ± 0.01	0.31 ± 0.02	0.25 ± 0.01	0.19 ± 0.01
4.99	0.07 ± 0.01	0.04 ± 0.01	0.00 ± 0.01	0.28 ± 0.01	0.19 ± 0.01	0.14 ± 0.01

Table 6.1

Semi-inclusive correlation function $C_n(\eta_1,\eta_2)$ at fixed η_1, at the energy $\sqrt{s}$ = 23 GeV. n_{obs} is the observed multiplicity and n_{true} is the corresponding mean true charged multiplicity. The correlation matrix has been symmetrized with respect to both diagonals.

η_2	$C_n(\eta_1,\eta_2)$ for n_{obs} = 10, 11 (n_{true} = 9.1)		
	η_1 = 0.0	η_1 = -0.87	η_1 = -1.96
-4.99	-0.018 ± 0.004	-0.030 ± 0.005	-0.021 ± 0.004
-4.82	-0.018 ± 0.005	-0.027 ± 0.006	-0.024 ± 0.004
-4.67	-0.031 ± 0.007	-0.044 ± 0.007	-0.048 ± 0.005
-4.53	-0.033 ± 0.008	-0.074 ± 0.008	-0.052 ± 0.007
-4.42	-0.048 ± 0.009	-0.070 ± 0.010	-0.053 ± 0.007
-4.29	-0.037 ± 0.009	-0.065 ± 0.009	-0.072 ± 0.007
-4.13	-0.056 ± 0.009	-0.102 ± 0.010	-0.094 ± 0.007
-3.96	-0.068 ± 0.010	-0.128 ± 0.010	-0.101 ± 0.008
-3.65	-0.077 ± 0.007	-0.092 ± 0.009	-0.081 ± 0.007
-3.21	-0.134 ± 0.009	-0.115 ± 0.011	-0.036 ± 0.009
-2.80	-0.195 ± 0.012	-0.136 ± 0.015	0.025 ± 0.012
-2.47	-0.262 ± 0.015	-0.114 ± 0.019	0.085 ± 0.016
-2.20	-0.305 ± 0.017	-0.064 ± 0.022	0.119 ± 0.018
-1.97	-0.349 ± 0.019	-0.050 ± 0.024	0.205 ± 0.021
-1.77	-0.353 ± 0.020	-0.062 ± 0.026	0.114 ± 0.021
-1.61	-0.360 ± 0.022	-0.029 ± 0.028	0.121 ± 0.023
-1.47	-0.377 ± 0.025	-0.049 ± 0.031	0.053 ± 0.025
-1.35	-0.390 ± 0.029	0.021 ± 0.037	0.030 ± 0.029
-0.87	-0.201 ± 0.026	0.194 ± 0.032	-0.020 ± 0.024
-0.61	-0.063 ± 0.024	0.084 ± 0.029	-0.170 ± 0.022
-0.32	0.050 ± 0.023	-0.028 ± 0.027	-0.257 ± 0.020
0.00	0.068 ± 0.023	-0.156 ± 0.026	-0.287 ± 0.019
0.32	0.050 ± 0.023	-0.309 ± 0.025	-0.337 ± 0.019
0.61	-0.063 ± 0.024	-0.504 ± 0.026	-0.422 ± 0.020
0.87	-0.201 ± 0.026	-0.650 ± 0.027	-0.526 ± 0.021
1.35	-0.390 ± 0.029	-0.715 ± 0.031	-0.517 ± 0.025
1.47	-0.377 ± 0.025	-0.584 ± 0.028	-0.450 ± 0.021
1.61	-0.360 ± 0.022	-0.589 ± 0.025	-0.430 ± 0.019
1.77	-0.353 ± 0.020	-0.583 ± 0.022	-0.447 ± 0.017
1.96	-0.349 ± 0.019	-0.539 ± 0.021	-0.363 ± 0.017
2.20	-0.305 ± 0.017	-0.405 ± 0.019	-0.285 ± 0.015
2.47	-0.262 ± 0.015	-0.330 ± 0.017	-0.210 ± 0.014
2.80	-0.195 ± 0.012	-0.248 ± 0.014	-0.138 ± 0.011
3.21	-0.134 ± 0.009	-0.115 ± 0.011	-0.040 ± 0.009
3.65	-0.077 ± 0.007	-0.030 ± 0.009	0.000 ± 0.007
3.96	-0.068 ± 0.010	-0.011 ± 0.012	0.002 ± 0.010
4.13	-0.056 ± 0.009	0.007 ± 0.012	0.000 ± 0.009
4.29	-0.037 ± 0.009	0.008 ± 0.011	0.016 ± 0.009
4.42	-0.048 ± 0.009	-0.015 ± 0.011	0.011 ± 0.009
4.53	-0.033 ± 0.008	0.003 ± 0.010	0.029 ± 0.009
4.67	-0.031 ± 0.007	-0.002 ± 0.009	0.001 ± 0.007
4.81	-0.018 ± 0.005	-0.018 ± 0.006	0.003 ± 0.005
4.99	-0.018 ± 0.004	0.000 ± 0.005	0.002 ± 0.004

Table 6.2

Semi-inclusive correlation function $C_n(\eta_1,\eta_2)$ at fixed η_1, at the energy $\sqrt{s}$ = 23 GeV. n_{obs} is the observed multiplicity and n_{true} is the corresponding mean true charged multiplicity. The correlation matrix has been symmetrized with respect to both diagonals.

η_2	$C_n(\eta_1,\eta_2)$ for n_{obs} = 14, 15 (n_{true} = 14.0)		
	η_1 = 0.0	η_1 = -0.87	η_1 = -1.96
-4.99	-0.019 ± 0.006	-0.029 ± 0.007	-0.029 ± 0.005
-4.82	-0.026 ± 0.007	-0.004 ± 0.010	-0.022 ± 0.006
-4.67	-0.037 ± 0.010	-0.057 ± 0.011	-0.039 ± 0.008
-4.53	-0.042 ± 0.012	-0.079 ± 0.013	-0.043 ± 0.010
-4.42	-0.055 ± 0.013	-0.088 ± 0.015	-0.071 ± 0.010
-4.29	-0.055 ± 0.013	-0.083 ± 0.014	-0.090 ± 0.010
-4.13	-0.086 ± 0.014	-0.124 ± 0.016	-0.088 ± 0.011
-3.96	-0.099 ± 0.015	-0.143 ± 0.018	-0.097 ± 0.013
-3.65	-0.097 ± 0.012	-0.124 ± 0.014	-0.087 ± 0.010
-3.21	-0.219 ± 0.017	-0.220 ± 0.020	-0.029 ± 0.016
-2.80	-0.347 ± 0.023	-0.249 ± 0.028	0.029 ± 0.022
-2.47	-0.433 ± 0.030	-0.234 ± 0.037	0.129 ± 0.029
-2.20	-0.537 ± 0.036	-0.147 ± 0.045	0.250 ± 0.035
-1.97	-0.668 ± 0.042	-0.235 ± 0.052	0.388 ± 0.042
-1.77	-0.698 ± 0.046	-0.106 ± 0.058	0.283 ± 0.045
-1.61	-0.644 ± 0.052	-0.002 ± 0.065	0.293 ± 0.050
-1.47	-0.743 ± 0.059	-0.124 ± 0.073	0.051 ± 0.055
-1.35	-0.671 ± 0.069	0.134 ± 0.085	0.039 ± 0.063
-0.87	-0.407 ± 0.059	0.354 ± 0.072	-0.111 ± 0.052
-0.61	-0.094 ± 0.055	0.376 ± 0.067	-0.228 ± 0.048
-0.32	0.158 ± 0.053	-0.114 ± 0.061	-0.518 ± 0.043
0.00	0.236 ± 0.052	-0.327 ± 0.059	-0.629 ± 0.042
0.32	0.158 ± 0.053	-0.500 ± 0.060	-0.595 ± 0.043
0.61	-0.094 ± 0.055	-0.878 ± 0.062	-0.786 ± 0.045
0.87	-0.407 ± 0.059	-1.356 ± 0.065	-0.966 ± 0.048
1.35	-0.671 ± 0.069	-1.377 ± 0.077	-0.970 ± 0.057
1.47	-0.743 ± 0.059	-1.156 ± 0.067	-0.783 ± 0.050
1.61	-0.644 ± 0.052	-1.195 ± 0.059	-0.692 ± 0.044
1.77	-0.698 ± 0.046	-0.963 ± 0.053	-0.552 ± 0.040
1.96	-0.668 ± 0.042	-0.849 ± 0.049	-0.529 ± 0.037
2.20	-0.537 ± 0.036	-0.744 ± 0.042	-0.375 ± 0.032
2.47	-0.433 ± 0.030	-0.434 ± 0.036	-0.205 ± 0.027
2.80	-0.347 ± 0.023	-0.297 ± 0.028	-0.099 ± 0.021
3.21	-0.219 ± 0.017	-0.172 ± 0.020	-0.004 ± 0.016
3.65	-0.097 ± 0.012	-0.035 ± 0.015	-0.010 ± 0.011
3.96	-0.099 ± 0.015	0.000 ± 0.020	0.053 ± 0.016
4.13	-0.086 ± 0.014	-0.024 ± 0.017	0.055 ± 0.014
4.29	-0.055 ± 0.013	-0.020 ± 0.016	0.032 ± 0.013
4.42	-0.055 ± 0.013	-0.013 ± 0.017	0.024 ± 0.013
4.53	-0.042 ± 0.012	-0.022 ± 0.015	0.013 ± 0.012
4.67	-0.037 ± 0.010	-0.013 ± 0.012	0.007 ± 0.010
4.81	-0.026 ± 0.007	-0.020 ± 0.009	-0.005 ± 0.007
4.99	-0.019 ± 0.006	-0.001 ± 0.008	0.001 ± 0.006

Table 6.3

Semi-inclusive correlation function $C_n(\eta_1,\eta_2)$ at fixed η_1, at the energy $\sqrt{s}$ = 23 GeV. n_{obs} is the observed multiplicity and n_{true} is the corresponding mean true charged multiplicity. The correlation matrix has been symmetrized with respect to both diagonals.

η_2	$C_n(\eta_1,\eta_2)$ for n_{obs} = 20, 21 (n_{true} = 21.7)		
	η_1 = 0.0	η_1 = -0.87	η_1 =1.96
-4.99	-0.026 ± 0.016	-0.029 ± 0.019	-0.006 ± 0.013
-4.82	-0.031 ± 0.024	-0.006 ± 0.029	0.022 ± 0.021
-4.67	-0.043 ± 0.030	-0.124 ± 0.030	-0.014 ± 0.024
-4.53	-0.065 ± 0.033	-0.155 ± 0.033	-0.063 ± 0.024
-4.42	-0.060 ± 0.041	-0.081 ± 0.046	-0.065 ± 0.030
-4.29	-0.135 ± 0.041	-0.171 ± 0.046	-0.065 ± 0.033
-4.13	-0.125 ± 0.038	-0.153 ± 0.043	-0.029 ± 0.031
-3.96	-0.178 ± 0.050	-0.261 ± 0.056	-0.073 ± 0.040
-3.65	-0.192 ± 0.036	-0.262 ± 0.041	-0.129 ± 0.028
-3.21	-0.425 ± 0.050	-0.484 ± 0.057	-0.095 ± 0.040
-2.80	-0.579 ± 0.073	-0.488 ± 0.085	0.039 ± 0.060
-2.47	-0.781 ± 0.097	-0.307 ± 0.115	0.198 ± 0.081
-2.20	-1.017 ± 0.129	-0.474 ± 0.116	0.392 ± 0.108
-1.97	-1.506 ± 0.163	-0.789 ± 0.193	0.417 ± 0.137
-1.77	-1.237 ± 0.183	-0.642 ± 0.215	0.312 ± 0.149
-1.61	-1.348 ± 0.211	-0.191 ± 0.251	0.362 ± 0.172
-1.47	-1.406 ± 0.254	-0.205 ± 0.301	-0.071 ± 0.202
-1.35	-0.982 ± 0.283	0.643 ± 0.337	0.474 ± 0.226
-0.87	-0.668 ± 0.253	0.874 ± 0.299	-0.479 ± 0.193
-0.61	-0.210 ± 0.238	0.391 ± 0.277	-0.674 ± 0.179
-0.32	0.405 ± 0.230	0.022 ± 0.261	-1.102 ± 0.167
0.00	0.753 ± 0.226	-0.112 ± 0.253	-0.970 ± 0.164
0.32	0.405 ± 0.230	-0.815 ± 0.256	-0.780 ± 0.169
0.61	-0.210 ± 0.238	-1.767 ± 0.265	-0.948 ± 0.177
0.87	-0.688 ± 0.253	-2.448 ± 0.279	-1.405 ± 0.187
1.35	-0.982 ± 0.283	-2.659 ± 0.312	-1.541 ± 0.208
1.47	-1.406 ± 0.254	-2.373 ± 0.285	-0.912 ± 0.194
1.61	-1.348 ± 0.211	-2.127 ± 0.237	-1.065 ± 0.160
1.77	-1.237 ± 0.183	-1.757 ± 0.207	-0.834 ± 0.140
1.96	-1.506 ± 0.163	-1.310 ± 0.190	-0.716 ± 0.127
2.20	-1.017 ± 0.129	-1.296 ± 0.147	-0.557 ± 0.100
2.47	-0.781 ± 0.097	-0.564 ± 0.113	-0.059 ± 0.078
2.80	-0.579 ± 0.073	-0.238 ± 0.087	-0.003 ± 0.059
3.21	-0.425 ± 0.050	-0.281 ± 0.059	-0.008 ± 0.042
3.65	-0.192 ± 0.036	-0.061 ± 0.044	0.078 ± 0.031
3.96	-0.178 ± 0.050	-0.037 ± 0.062	0.087 ± 0.045
4.13	-0.125 ± 0.038	-0.112 ± 0.045	-0.012 ± 0.032
4.29	-0.135 ± 0.041	-0.012 ± 0.054	0.074 ± 0.039
4.42	-0.060 ± 0.041	-0.028 ± 0.049	0.039 ± 0.036
4.53	-0.065 ± 0.033	0.050 ± 0.044	0.019 ± 0.029
4.67	-0.043 ± 0.030	0.005 ± 0.037	0.011 ± 0.025
4.81	-0.031 ± 0.024	-0.070 ± 0.025	0.006 ± 0.019
4.99	-0.026 ± 0.016	-0.016 ± 0.020	0.004 ± 0.002

Table 7.1

Semi-inclusive correlation function $C_n(\eta_1,\eta_2)$ at fixed η_1, at the energy $\sqrt{s}$ = 62 GeV. n_{obs} is the observed multiplicity and n_{true} is the corresponding mean true charged multiplicity. The correlation matrix has been symmetrized with respect to both diagonals.

η_2	$C_n(\eta_1,\eta_2)$ for n_{obs} = 10, 11 (n_{true} = 8.1)		
	η_1 = 0.0	η_1 = -0.87	η_1 = -1.96
-4.99	-0.032 ± 0.007	-0.051 ± 0.009	-0.061 ± 0.007
-4.82	-0.042 ± 0.009	-0.066 ± 0.010	-0.074 ± 0.008
-4.67	-0.041 ± 0.010	-0.082 ± 0.012	-0.060 ± 0.010
-4.53	-0.070 ± 0.011	-0.075 ± 0.013	-0.083 ± 0.011
-4.42	-0.070 ± 0.013	-0.097 ± 0.015	-0.042 ± 0.014
-4.29	-0.103 ± 0.011	-0.088 ± 0.014	-0.046 ± 0.012
-4.13	-0.117 ± 0.012	-0.102 ± 0.015	-0.030 ± 0.013
-3.96	-0.141 ± 0.011	-0.115 ± 0.014	-0.037 ± 0.013
-3.65	-0.139 ± 0.008	-0.062 ± 0.011	0.050 ± 0.010
-3.21	-0.191 ± 0.009	-0.050 ± 0.012	0.108 ± 0.011
-2.80	-0.220 ± 0.010	-0.088 ± 0.013	0.148 ± 0.013
-2.47	-0.226 ± 0.011	-0.046 ± 0.015	0.172 ± 0.014
-2.20	-0.216 ± 0.012	-0.019 ± 0.016	0.206 ± 0.015
-1.97	-0.211 ± 0.013	0.066 ± 0.019	0.228 ± 0.017
-1.77	-0.189 ± 0.015	0.056 ± 0.020	0.214 ± 0.018
-1.61	-0.135 ± 0.016	0.080 ± 0.021	0.182 ± 0.019
-1.47	-0.139 ± 0.018	0.147 ± 0.024	0.156 ± 0.021
-1.35	-0.115 ± 0.021	0.150 ± 0.028	0.091 ± 0.023
-0.87	-0.017 ± 0.018	0.271 ± 0.023	0.090 ± 0.019
-0.61	0.088 ± 0.017	0.214 ± 0.021	-0.036 ± 0.016
-0.32	0.138 ± 0.016	0.103 ± 0.019	-0.103 ± 0.014
0.00	0.203 ± 0.016	-0.023 ± 0.017	-0.168 ± 0.013
0.32	0.138 ± 0.016	-0.085 ± 0.017	-0.224 ± 0.013
0.61	0.088 ± 0.017	-0.185 ± 0.018	-0.301 ± 0.014
0.87	-0.017 ± 0.018	-0.231 ± 0.019	-0.341 ± 0.015
1.35	-0.115 ± 0.021	-0.373 ± 0.022	-0.393 ± 0.018
1.47	-0.139 ± 0.018	-0.372 ± 0.019	-0.360 ± 0.015
1.61	-0.135 ± 0.016	-0.373 ± 0.017	-0.348 ± 0.014
1.77	-0.189 ± 0.015	-0.380 ± 0.016	-0.371 ± 0.013
1.96	-0.211 ± 0.013	-0.390 ± 0.015	-0.351 ± 0.012
2.20	-0.216 ± 0.012	-0.390 ± 0.013	-0.328 ± 0.011
2.47	-0.226 ± 0.011	-0.385 ± 0.012	-0.346 ± 0.010
2.80	-0.220 ± 0.010	-0.361 ± 0.011	-0.316 ± 0.009
3.21	-0.191 ± 0.009	-0.312 ± 0.010	-0.261 ± 0.008
3.65	-0.139 ± 0.008	-0.215 ± 0.009	-0.164 ± 0.008
3.96	-0.141 ± 0.011	-0.171 ± 0.013	-0.143 ± 0.011
4.13	-0.117 ± 0.012	-0.128 ± 0.014	-0.119 ± 0.012
4.29	-0.103 ± 0.011	-0.093 ± 0.014	-0.095 ± 0.012
4.42	-0.070 ± 0.013	-0.114 ± 0.015	-0.039 ± 0.014
4.53	-0.070 ± 0.011	-0.092 ± 0.013	-0.041 ± 0.012
4.67	-0.041 ± 0.010	-0.057 ± 0.012	-0.022 ± 0.011
4.81	-0.042 ± 0.009	-0.040 ± 0.011	-0.005 ± 0.010
4.99	-0.032 ± 0.007	-0.018 ± 0.009	0.005 ± 0.008

Table 7.2

Semi-inclusive correlation function $C_n(\eta_1,\eta_2)$ at fixed η_1, at the energy $\sqrt{s}$ = 62 GeV. n_{obs} is the observed multiplicity and n_{true} is the corresponding mean true charged multiplicity. The correlation matrix has been symmetrized with respect to both diagonals.

η_2	$C_n(\eta_1,\eta_2)$ for n_{obs} = 20, 21 (n_{true} = 18.8)		
	η_1 = 0.0	η_1 = -0.87	η_1 = -1.96
-4.99	-0.070 ± 0.011	-0.116 ± 0.013	-0.120 ± 0.011
-4.82	-0.066 ± 0.015	-0.141 ± 0.018	-0.118 ± 0.015
-4.67	-0.100 ± 0.019	-0.118 ± 0.022	-0.127 ± 0.019
-4.53	-0.155 ± 0.021	-0.131 ± 0.026	-0.185 ± 0.022
-4.42	-0.152 ± 0.025	-0.155 ± 0.031	-0.161 ± 0.026
-4.29	-0.128 ± 0.023	-0.187 ± 0.028	-0.151 ± 0.024
-4.13	-0.194 ± 0.025	-0.237 ± 0.029	-0.172 ± 0.025
-3.96	-0.242 ± 0.025	-0.272 ± 0.030	-0.168 ± 0.026
-3.65	-0.220 ± 0.020	-0.164 ± 0.024	-0.003 ± 0.021
-3.21	-0.395 ± 0.025	-0.138 ± 0.031	0.225 ± 0.027
-2.80	-0.526 ± 0.031	-0.140 ± 0.038	0.392 ± 0.034
-2.47	-0.639 ± 0.037	-0.082 ± 0.047	0.662 ± 0.043
-2.20	-0.651 ± 0.042	0.123 ± 0.053	0.779 ± 0.048
-1.97	-0.725 ± 0.046	0.197 ± 0.058	0.941 ± 0.053
-1.77	-0.690 ± 0.049	0.380 ± 0.063	0.874 ± 0.056
-1.61	-0.607 ± 0.053	0.446 ± 0.068	0.690 ± 0.060
-1.47	-0.570 ± 0.059	0.404 ± 0.075	0.433 ± 0.065
-1.35	-0.447 ± 0.068	0.630 ± 0.086	0.646 ± 0.074
-0.87	-0.108 ± 0.056	0.700 ± 0.070	0.206 ± 0.058
-0.61	0.143 ± 0.052	0.638 ± 0.064	-0.015 ± 0.053
-0.32	0.304 ± 0.049	0.141 ± 0.058	-0.407 ± 0.048
0.00	0.489 ± 0.048	-0.041 ± 0.056	-0.503 ± 0.046
0.32	0.304 ± 0.049	-0.281 ± 0.057	-0.668 ± 0.047
0.61	0.143 ± 0.052	-0.861 ± 0.059	-0.942 ± 0.049
0.87	-0.108 ± 0.056	-1.077 ± 0.064	-1.336 ± 0.053
1.35	-0.447 ± 0.068	-1.555 ± 0.076	-1.525 ± 0.064
1.47	-0.570 ± 0.059	-1.545 ± 0.067	-1.362 ± 0.057
1.61	-0.607 ± 0.053	-1.404 ± 0.061	-1.352 ± 0.051
1.77	-0.690 ± 0.049	-1.492 ± 0.056	-1.410 ± 0.047
1.96	-0.725 ± 0.046	-1.512 ± 0.052	-1.303 ± 0.044
2.20	-0.651 ± 0.042	-1.215 ± 0.048	-1.111 ± 0.041
2.47	-0.639 ± 0.037	-1.125 ± 0.043	-0.980 ± 0.037
2.80	-0.526 ± 0.031	-0.833 ± 0.036	-0.720 ± 0.031
3.21	-0.395 ± 0.025	-0.550 ± 0.029	-0.461 ± 0.025
3.65	-0.220 ± 0.020	-0.278 ± 0.023	-0.184 ± 0.020
3.96	-0.242 ± 0.025	-0.224 ± 0.030	-0.133 ± 0.026
4.13	-0.194 ± 0.025	-0.227 ± 0.029	-0.087 ± 0.026
4.29	-0.128 ± 0.023	-0.120 ± 0.028	-0.075 ± 0.024
4.42	-0.152 ± 0.025	-0.080 ± 0.031	-0.012 ± 0.028
4.53	-0.155 ± 0.021	-0.148 ± 0.026	-0.030 ± 0.023
4.67	-0.100 ± 0.019	-0.083 ± 0.023	0.011 ± 0.020
4.81	-0.066 ± 0.015	-0.037 ± 0.019	0.018 ± 0.017
4.99	-0.070 ± 0.011	-0.010 ± 0.015	-0.010 ± 0.013

Table 7.3

Semi-inclusive correlation function $C_n(\eta_1,\eta_2)$ at fixed η_1, at the energy $\sqrt{s}$ = 62 GeV. n_{obs} is the observed multiplicity and n_{true} is the corresponding mean true charged multiplicity. The correlation matrix has been symmetrized with respect to both diagonals.

η_2	$C_n(\eta_1,\eta_2)$ for n_{obs} = 30, 31 (n_{true} = 30.8)		
	η_1 = 0.0	η_1 = -0.87	η_1 = -1.96
-4.99	-0.085 ± 0.035	-0.129 ± 0.041	-0.105 ± 0.033
-4.82	-0.127 ± 0.034	-0.256 ± 0.037	-0.171 ± 0.031
-4.67	-0.248 ± 0.046	-0.307 ± 0.053	-0.234 ± 0.044
-4.53	-0.188 ± 0.059	-0.220 ± 0.069	-0.196 ± 0.057
-4.42	-0.294 ± 0.065	-0.433 ± 0.074	-0.207 ± 0.064
-4.29	-0.308 ± 0.059	-0.410 ± 0.069	-0.292 ± 0.057
-4.13	-0.328 ± 0.064	-0.489 ± 0.074	-0.358 ± 0.061
-3.96	-0.345 ± 0.065	-0.413 ± 0.076	-0.186 ± 0.064
-3.65	-0.444 ± 0.048	-0.413 ± 0.058	-0.292 ± 0.048
-3.21	-0.867 ± 0.072	-0.549 ± 0.086	-0.118 ± 0.073
-2.80	-1.090 ± 0.101	-0.678 ± 0.121	0.198 ± 0.103
-2.47	-1.054 ± 0.127	-0.209 ± 0.153	0.623 ± 0.130
-2.20	-1.306 ± 0.148	-0.010 ± 0.180	0.983 ± 0.153
-1.97	-1.333 ± 0.171	0.717 ± 0.211	1.067 ± 0.176
-1.77	-1.304 ± 0.189	0.913 ± 0.232	1.843 ± 0.196
-1.61	-1.238 ± 0.204	0.739 ± 0.250	1.025 ± 0.208
-1.47	-1.207 ± 0.222	0.919 ± 0.272	1.014 ± 0.226
-1.35	-0.934 ± 0.245	1.491 ± 0.300	1.080 ± 0.247
-0.87	-0.188 ± 0.213	1.745 ± 0.258	0.842 ± 0.211
-0.61	0.147 ± 0.196	1.123 ± 0.234	-0.165 ± 0.189
-0.32	0.993 ± 0.189	0.332 ± 0.219	-0.467 ± 0.177
0.00	0.852 ± 0.186	-0.015 ± 0.215	-0.871 ± 0.173
0.32	0.993 ± 0.189	-0.107 ± 0.217	-1.013 ± 0.175
0.61	0.147 ± 0.196	-1.457 ± 0.224	-1.508 ± 0.183
0.87	-0.188 ± 0.213	-2.555 ± 0.241	-2.291 ± 0.197
1.35	-0.934 ± 0.245	-3.044 ± 0.278	-2.520 ± 0.228
1.47	-1.207 ± 0.222	-3.008 ± 0.253	-2.695 ± 0.207
1.61	-1.238 ± 0.204	-2.836 ± 0.234	-2.473 ± 0.191
1.77	-1.304 ± 0.189	-3.496 ± 0.212	-2.857 ± 0.174
1.96	-1.333 ± 0.171	-2.632 ± 0.196	-2.134 ± 0.161
2.20	-1.306 ± 0.148	-2.457 ± 0.170	-1.586 ± 0.141
2.47	-1.054 ± 0.127	-1.839 ± 0.146	-1.355 ± 0.121
2.80	-1.090 ± 0.101	-1.179 ± 0.119	-0.790 ± 0.099
3.21	-0.867 ± 0.072	-0.914 ± 0.084	-0.580 ± 0.070
3.65	-0.444 ± 0.048	-0.488 ± 0.057	-0.220 ± 0.048
3.96	-0.345 ± 0.065	-0.353 ± 0.077	-0.167 ± 0.065
4.13	-0.328 ± 0.064	-0.217 ± 0.077	0.031 ± 0.066
4.29	-0.308 ± 0.059	-0.291 ± 0.071	-0.100 ± 0.060
4.42	-0.294 ± 0.065	-0.289 ± 0.077	-0.105 ± 0.066
4.53	-0.188 ± 0.059	-0.125 ± 0.071	0.044 ± 0.061
4.67	-0.248 ± 0.046	-0.270 ± 0.054	-0.102 ± 0.047
4.81	-0.127 ± 0.034	-0.185 ± 0.039	-0.045 ± 0.034
4.99	-0.085 ± 0.035	-0.081 ± 0.042	-0.081 ± 0.034

Figure captions

Fig. 1 : Layout of the experiment showing the location of hodoscopes H_1, H_2, H_3, H_4, TB, and L.

Fig. 2 : Hodoscope structure showing the subdivision into polar and azimuthal regions of H_1, H_2, H_3, H_4 (ϕ-hodoscopes), and of $H_2\theta$, $H_4\theta$ (θ-hodoscopes).

Fig. 3 : Single-particle density versus η at $\sqrt{s}$ = 23 GeV.

■: (H_4). ●: (H_2 + L). Raw data from this experiment.

□: (H_4). ○: (H_2 + L). Results of our Monte Carlo calculation using, as input, data from ISR[19] and FNAL[20].

a) Inclusive distribution $\rho^{(1)}(\eta)$.

b) Semi-inclusive distribution $\rho_n^{(1)}(\eta)$, with n = observed multiplicity = 14, 15, 16.

Fig. 4 : Uncorrected multiplicity distribution P_n versus n = observed multiplicity at $\sqrt{s}$ = 23 GeV.

●: Data from this experiment.

○: Results from the Monte Carlo calculation using, as input, data from FNAL[21].

The solid line shows the shape of the input multiplicity distribution from which the Monte Carlo results were obtained.

Fig. 5 : Fraction of events P_m of true charge multiplicity m which contribute to events of fixed observed multiplicity n. The arrow indicates the value of the observed multiplicity which is n = 14, 15 in (a) and n = 30, 31 in (b). The data are from the Monte Carlo calculation at $\sqrt{s}$ = 62 GeV.

Fig. 6 : Inclusive two-particle correlation function $C(\eta_1,\eta_2)$ versus η_2 at $\eta_1 = 0$.

a) $\sqrt{s}$ = 23 GeV; b) $\sqrt{s}$ = 62 GeV.

Fig. 7 : Semi-inclusive single-particle densities $\rho_n^{(1)}(\eta)$ versus η. The errors shown are systematic and arise from the uncertainty in the Monte Carlo calculation of efficiencies. Statistical errors are negligible.

a) $\sqrt{s}$ = 23 GeV.

▼: observed n = 10, 11 (true n = 9.1)

□: observed n = 14, 15 (true n = 14.0)

●: observed n = 20, 21 (true n = 21.7).

Fig. 7 : b) $\sqrt{s}$ = 62 GeV.
▼ : observed n = 10, 11 (true n = 8.1)
□ : observed n = 20, 21 (true n = 18.8)
● : observed n = 30, 31 (true n = 30.8).

Fig. 8 : Semi-inclusive correlations, $C_n(\eta_1,\eta_2)$, versus η_2 for fixed η_1 at $\sqrt{s}$ = 23 GeV.
a) η_1 = 0; b) η_1 = -0.87; c) η_1 = -1.96.
▼: observed n = 10, 11 (true n = 9.1)
□: observed n = 14, 15 (true n = 14.0)
●: observed n = 20, 21 (true n = 21.7).

Fig. 9 : Semi-inclusive correlations, $C_n(\eta_1,\eta_2)$, versus η_2 for fixed η_1 at $\sqrt{s}$ = 62 GeV.
a) η_1 = 0; b) η_1 = -0.87; c) η_1 = -1.96.
▼: observed n = 10, 11 (true n = 8.1)
□: observed n = 20, 21 (true n = 18.8)
●: observed n = 30, 31 (true n = 30.8).

Fig. 10 : Short-range part of the inclusive correlation function $\sum_n \alpha_n C_n(\eta_1,\eta_2)$ and long-range "crossed term", $\sum_n \alpha_n [\rho^{(1)}(\eta_1) - \rho_n^{(1)}(\eta_1)][\rho^{(1)}(\eta_2) - \rho_n^{(1)}(\eta_2)]$, both versus η_2 for η_1 = 0. The decomposition of $C(\eta_1,\eta_2)$ refers to Eq. (9) of the text.
a) $\sqrt{s}$ = 23 GeV; b) $\sqrt{s}$ = 62 GeV.
●: short-range correlation
□: long-range "crossed term".

Fig. 11 : Correlation function $C^{II}(\eta_1 - \eta_2)$ versus the rapidity difference $(\eta_1 - \eta_2)$. This correlation function is defined in Eq. (20) of the text.
a) $\sqrt{s}$ = 23 GeV; b) $\sqrt{s}$ = 62 GeV.
●: Data from this experiment
□: Data from Ref. 18.

Fig. 12 : $A_n/\rho_n^{(1)}(0)$ versus true charged multiplicity n. The coefficient A_n is defined in Eq. (23) of the text. The quoted errors are as derived from the best fit procedure to the C_n data.
●: $\sqrt{s}$ = 23 GeV
□: $\sqrt{s}$ = 62 GeV.

Fig. 13 : B_n versus true charged multiplicity n. The coefficient B_n is defined in Eq. (23) of the text. The quoted errors are as derived from the best fit procedure to the C_n data.

●: $\sqrt{s}$ = 23 GeV

□: $\sqrt{s}$ = 62 GeV.

Fig. 14 : $A_n/\rho_n^{(1)}(0)$ versus $n/\langle n\rangle$. A_n is defined in Eq. (23) of the text and n is the true charged multiplicity.

●: $\sqrt{s}$ = 23 GeV

□: $\sqrt{s}$ = 62 GeV.

Fig. 15 : B_n versus $n/\langle n\rangle$. B_n is defined in Eq. (23) of the text and n is the true charged multiplicity.

●: $\sqrt{s}$ = 23 GeV

□: $\sqrt{s}$ = 62 GeV.

Fig. 16 : The short-range part of the semi-inclusive correlation $C_n^*(\eta_1,\eta_2)$ versus η_2 with $\eta_1 = 0$. $C_n^*(\eta_1,\eta_2)$ is defined in Eq. (24) of the text. The solid line represents the Gaussian function, $A_n \exp\left[-\eta^2/2\delta^2\right]$ with $\delta = 0.85$ which is discussed in the text. n is the observed charged multiplicity.

a) $\sqrt{s}$ = 23 GeV.

▲: n = 10, 11

□: n = 14, 15

●: n = 20, 21.

b) $\sqrt{s}$ = 62 GeV.

▲: n = 10, 11

□: n = 20, 21

●: n = 30, 31.

Fig. 17 : Cluster moment $\langle k(k-1)\rangle/\langle k\rangle$ versus $n/\langle n\rangle$. k is the cluster decay multiplicity and n is the true charged multiplicity. (See text for discussion.)

●: $\sqrt{s}$ = 23 GeV

□: $\sqrt{s}$ = 62 GeV.

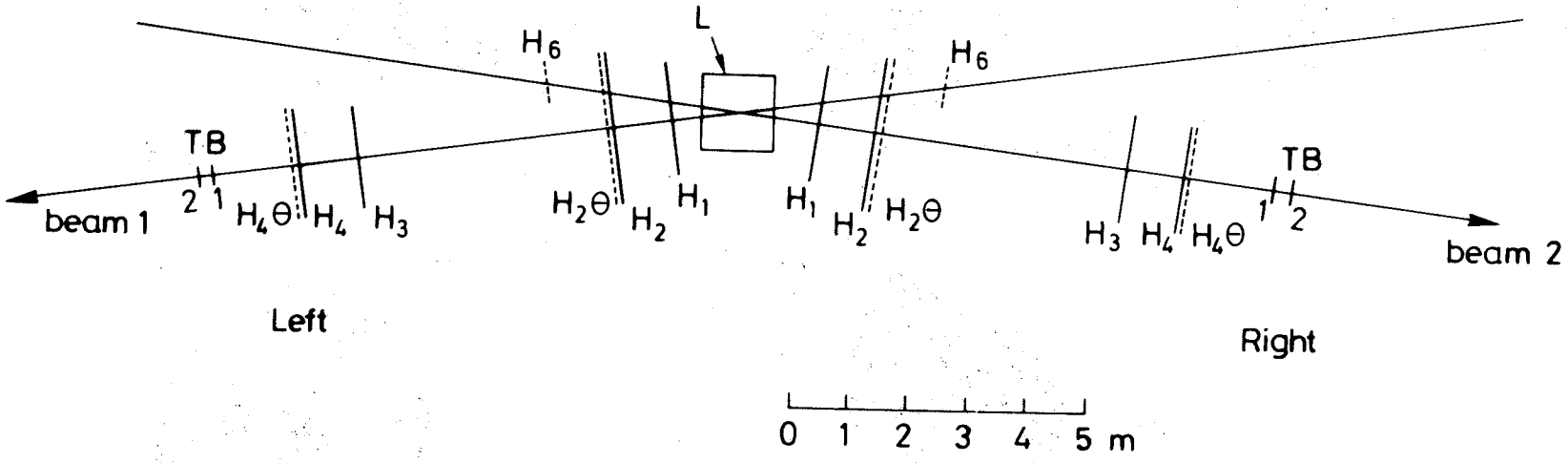
L
H6
H6
TB
TB
2
1
1
2
H4Θ
H4
H3
H2Θ
H2
H1
H1
H2
H2Θ
H3
H4
H4Θ
beam 1
beam 2
Left
Right
0 1 2 3 4 5 m

Fig. 1

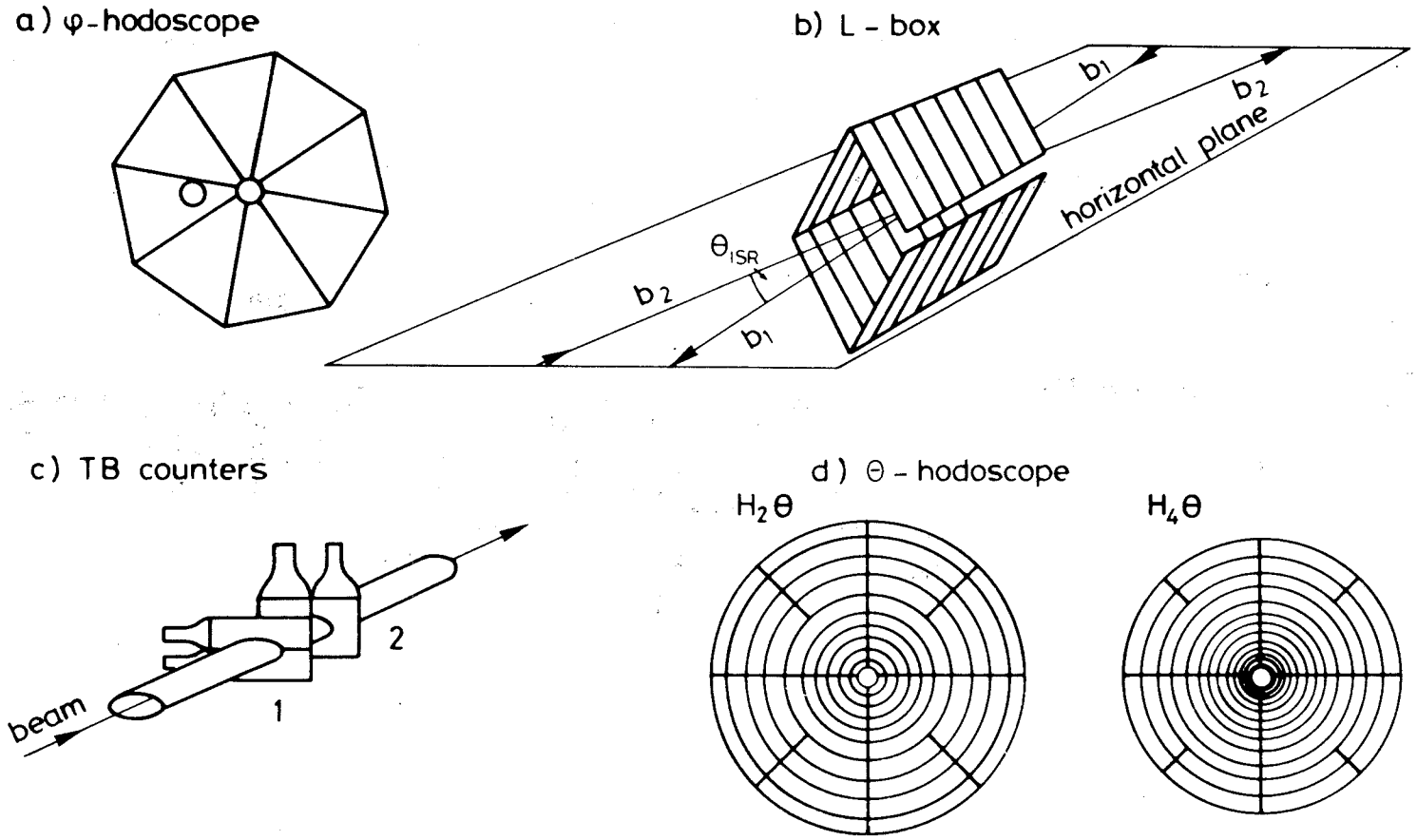
a) φ-hodoscope
b) L - box
b1
b2
horizontal plane
θISR
b2
b1
c) TB counters
beam
1
2
d) Θ - hodoscope
H2Θ
H4Θ

Fig. 2

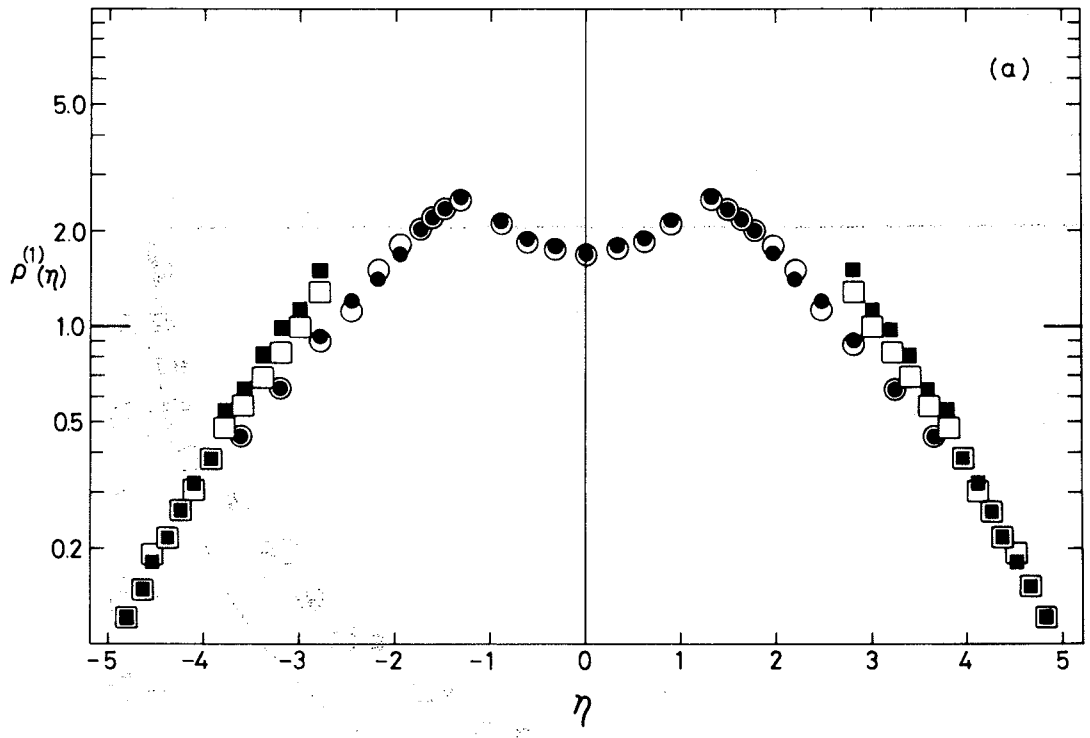
(a)
5.0
2.0
1.0
0.5
0.2
$\rho^{(1)}(\eta)$
-5
-4
-3
-2
-1
0
1
2
3
4
5
η

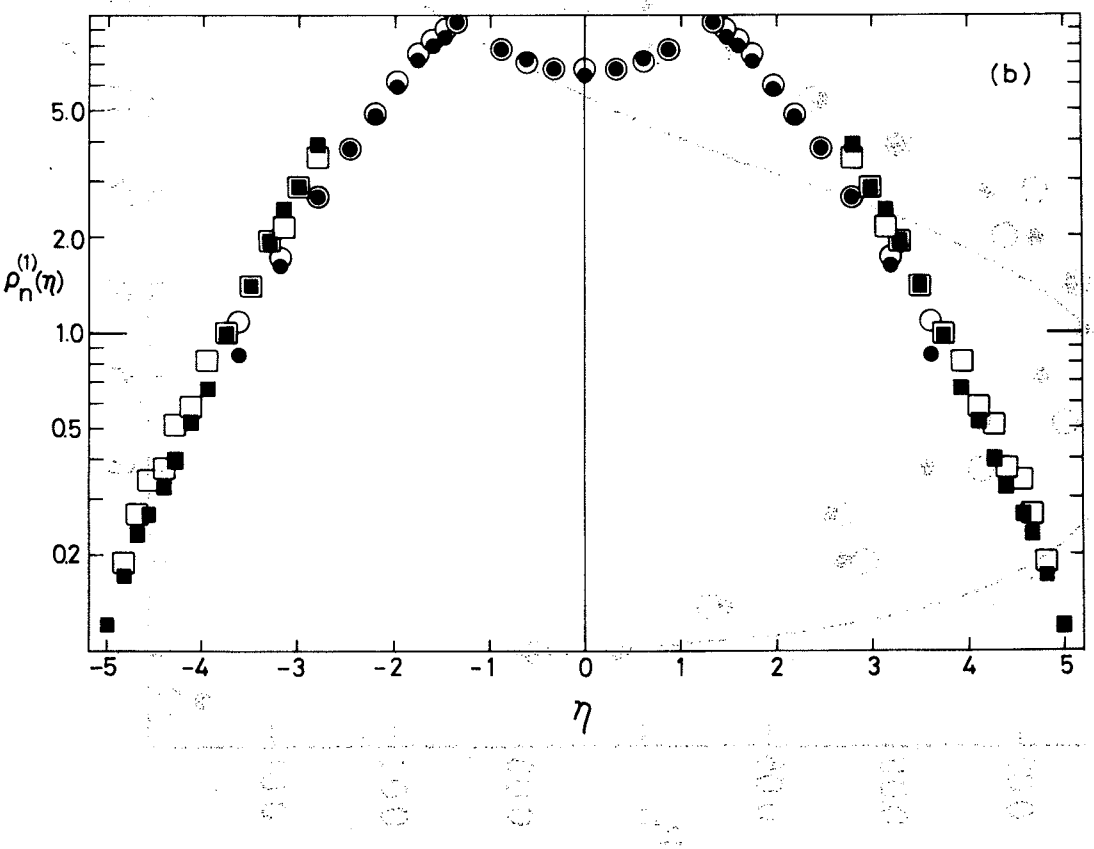
(b)
5.0
2.0
1.0
0.5
0.2
$\rho_n^{(1)}(\eta)$
-5
-4
-3
-2
-1
0
1
2
3
4
5
η

Fig. 3

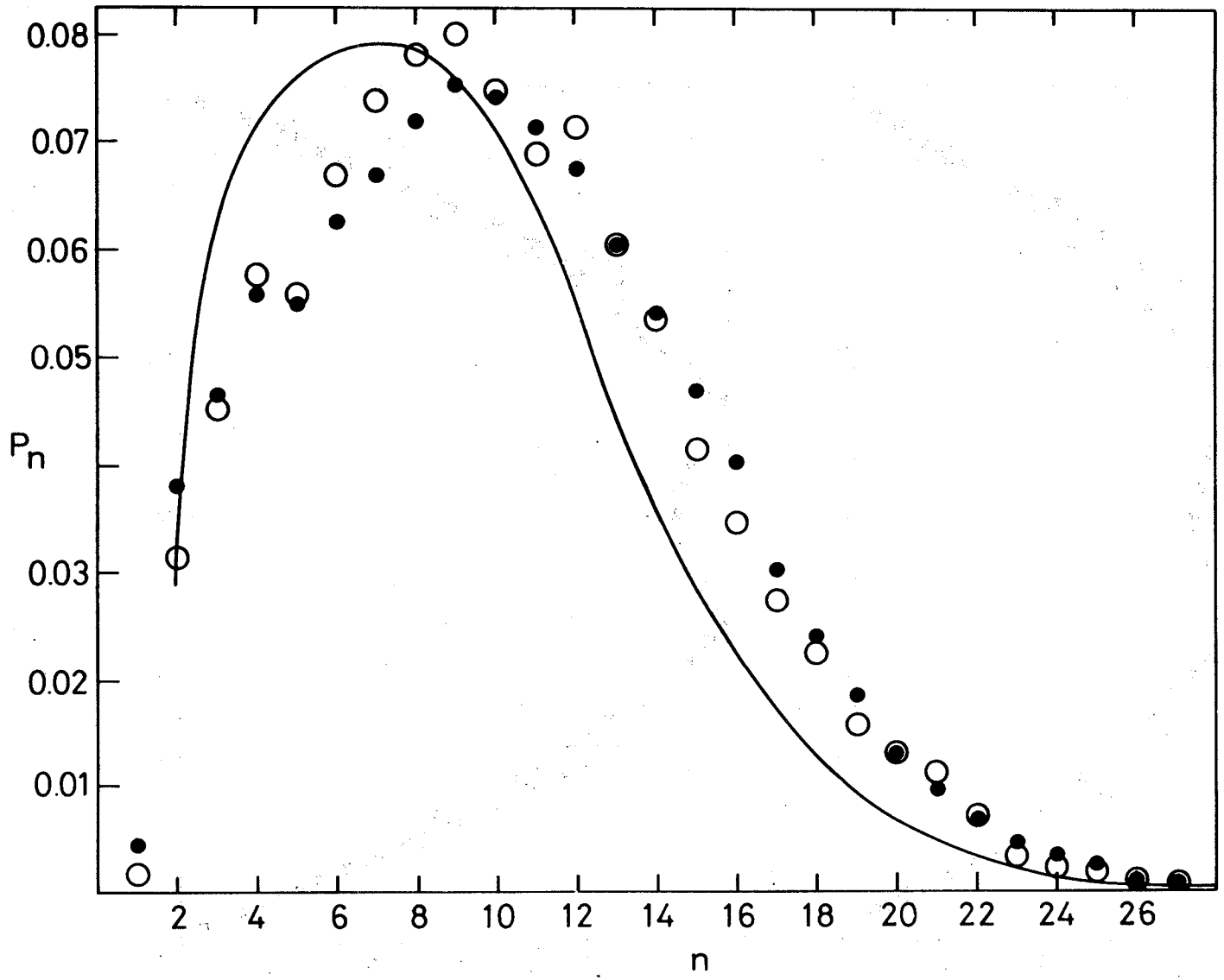

Fig. 4

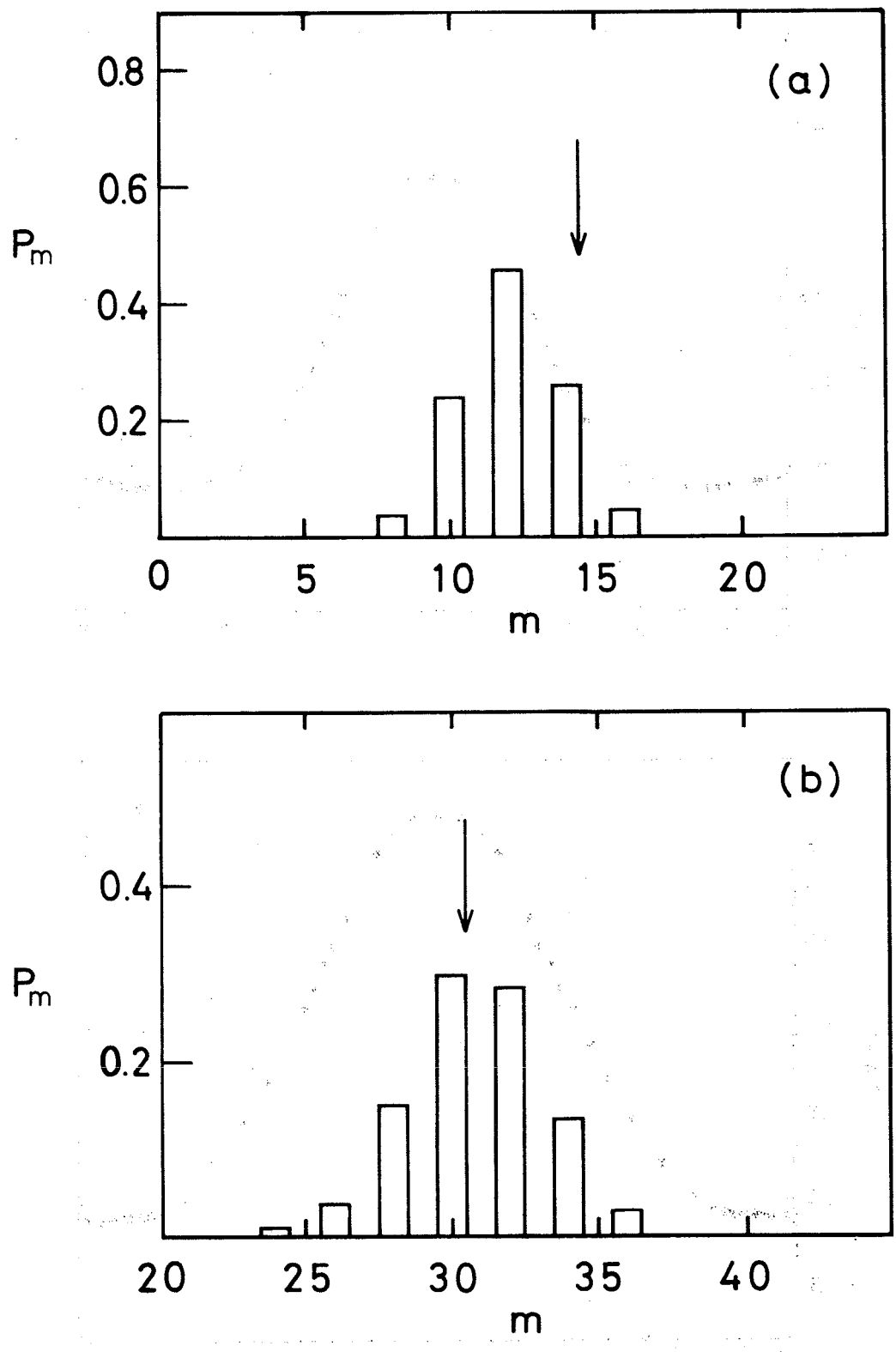

Fig. 5

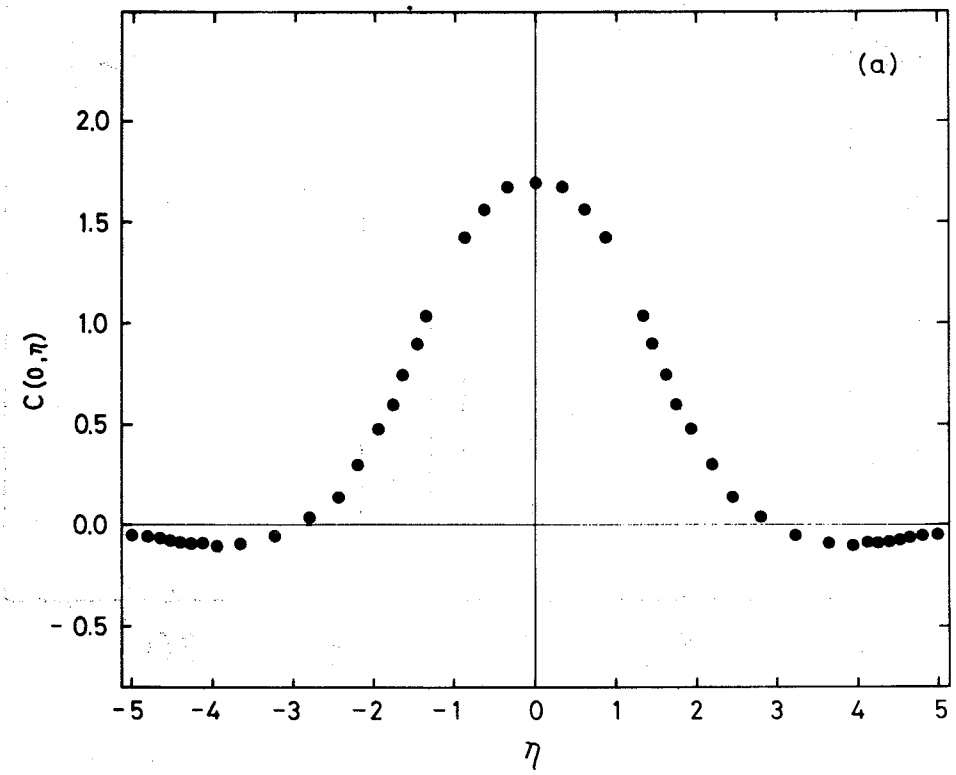
(a)
2.0
1.5
1.0
0.5
0.0
- 0.5
C(0,η)
-5 -4 -3 -2 -1 0 1 2 3 4 5
η

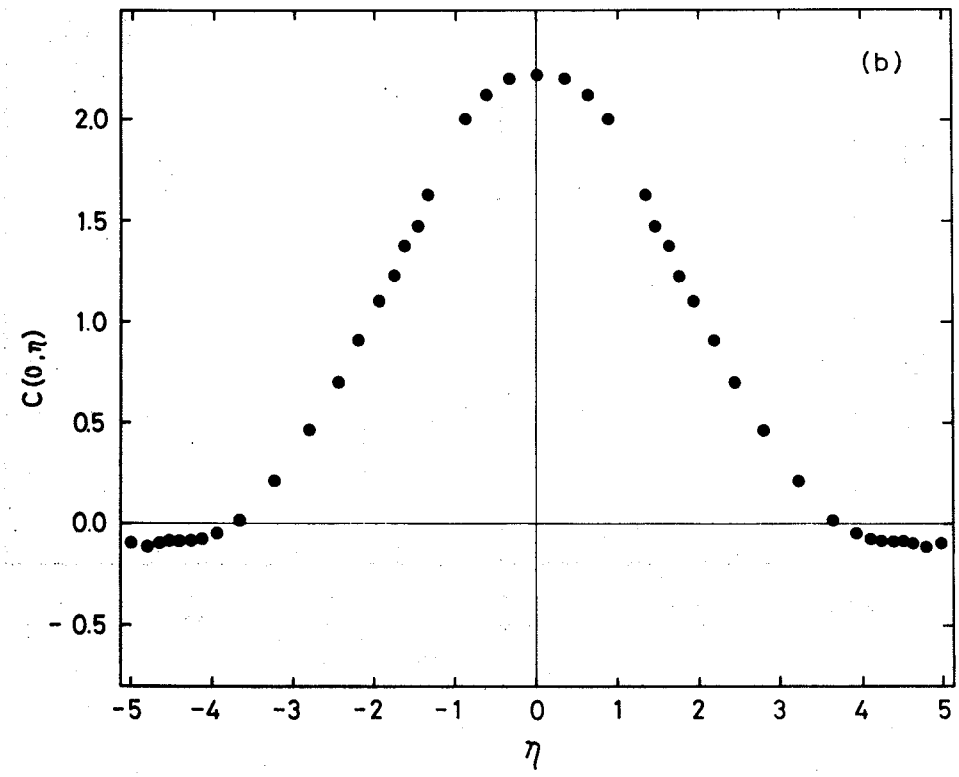
(b)
2.0
1.5
1.0
0.5
0.0
- 0.5
C(0,η)
-5 -4 -3 -2 -1 0 1 2 3 4 5
η

Fig. 6

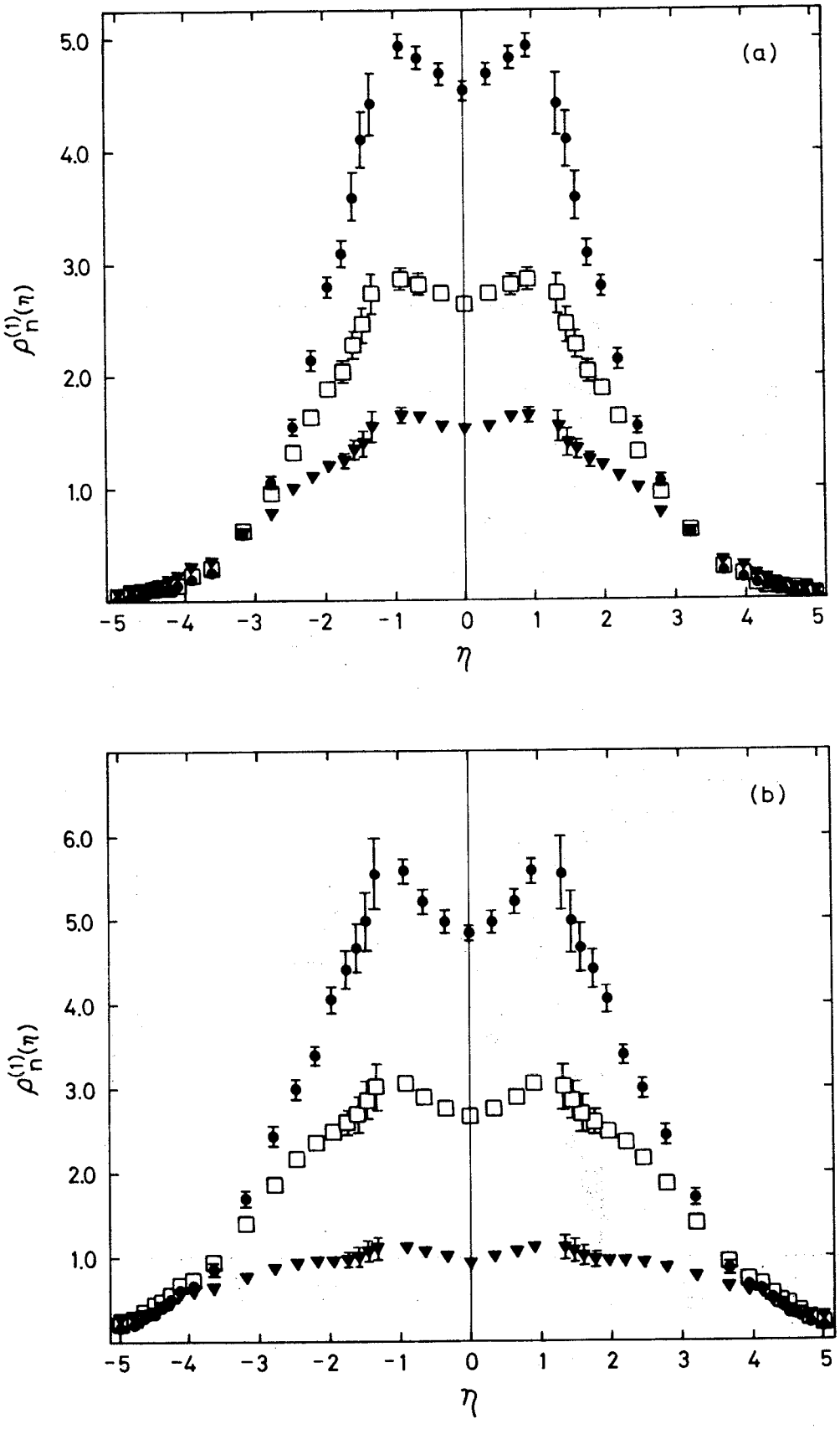

Fig. 7

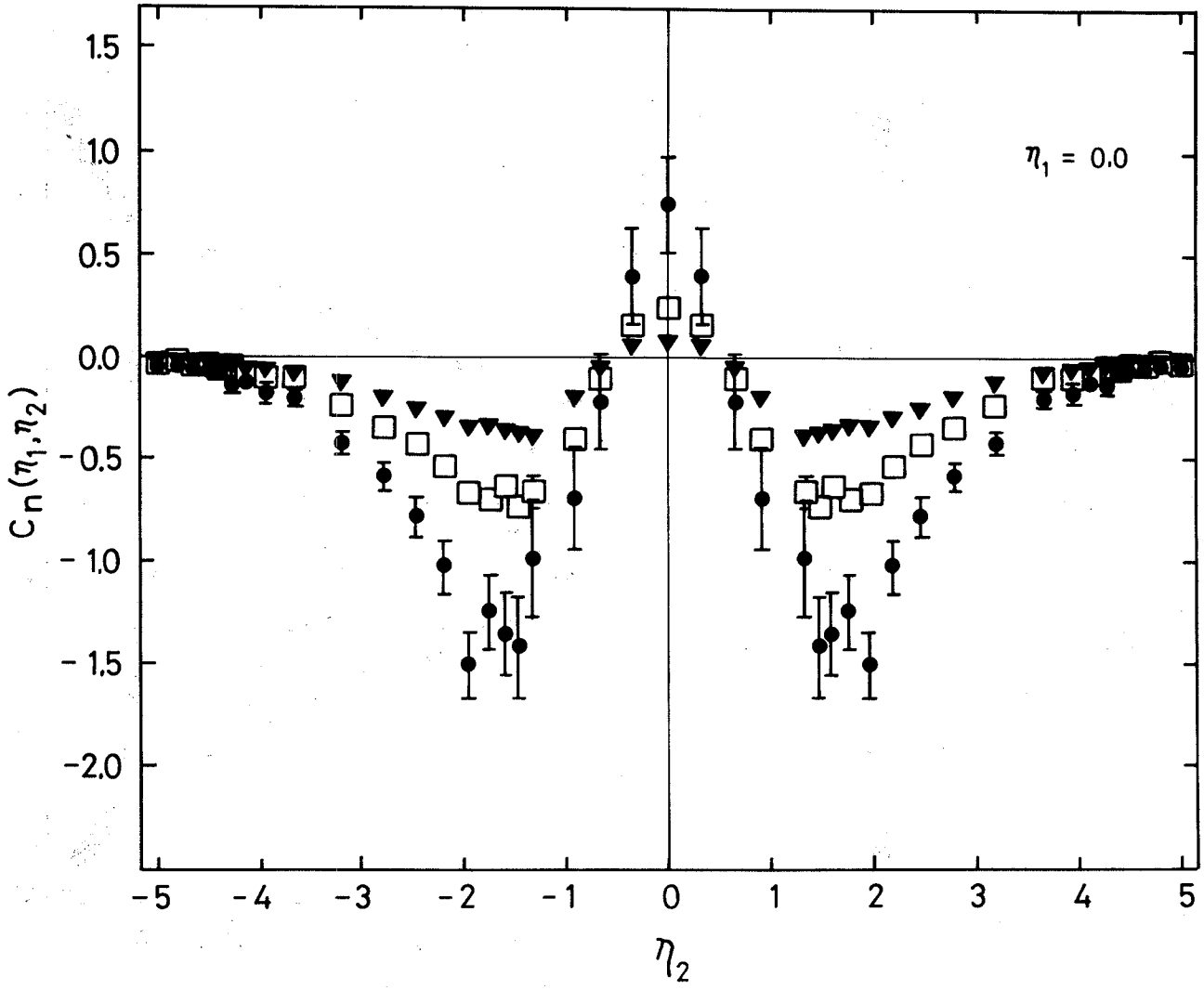

Fig. 8a

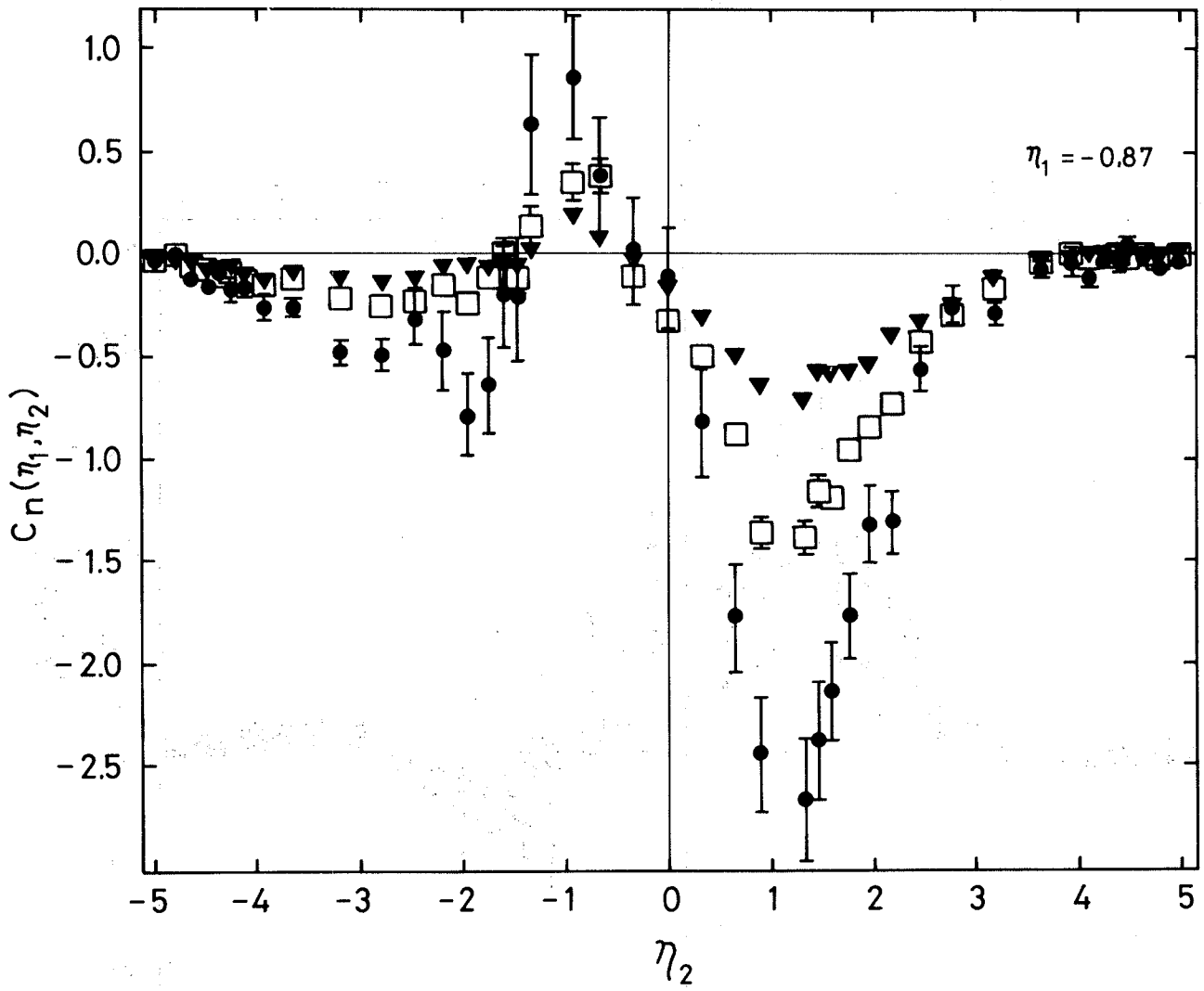

Fig. 8b

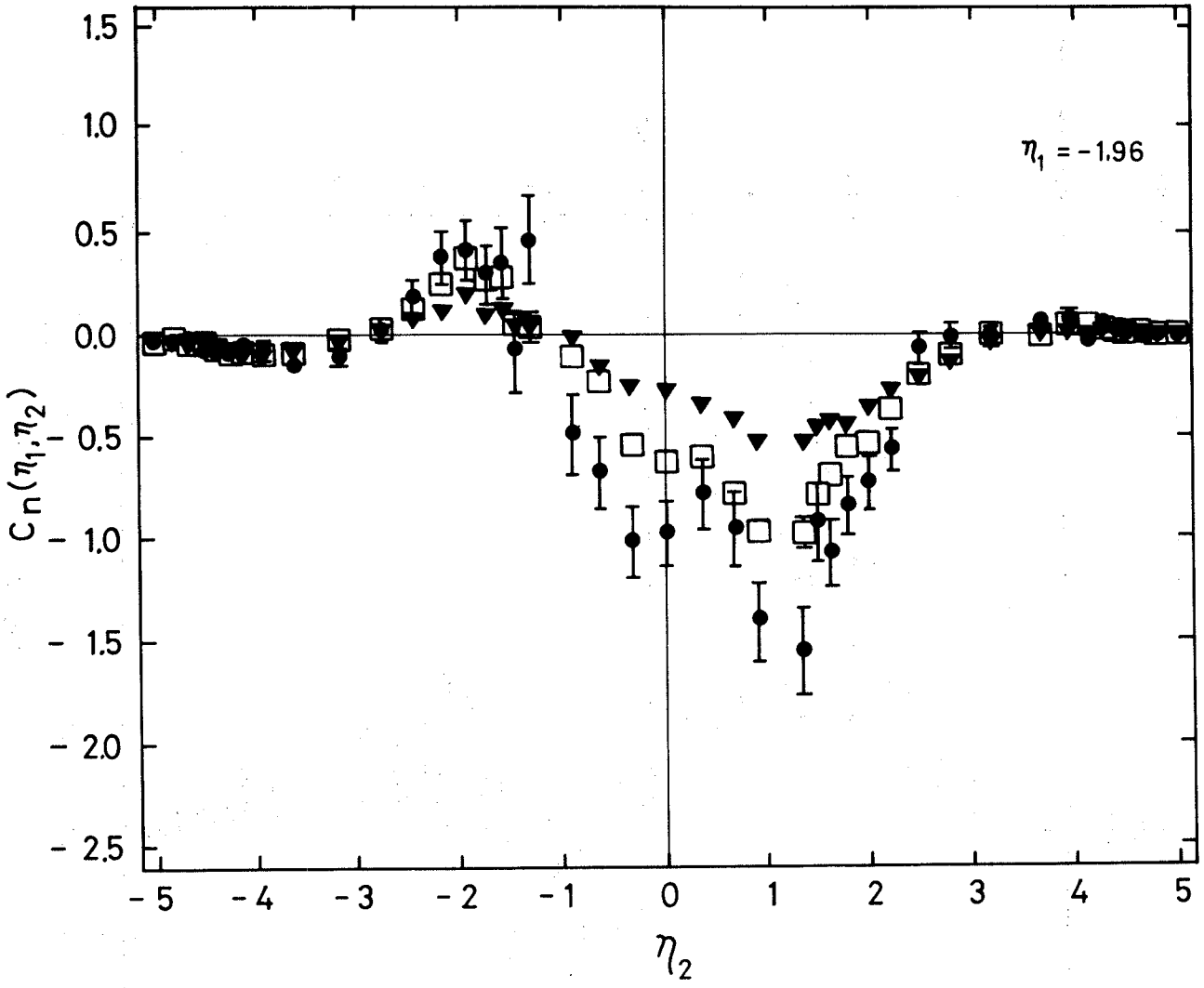
1.5
1.0
0.5
0.0
- 0.5
- 1.0
- 1.5
- 2.0
- 2.5
$C_n(\eta_1,\eta_2)$
$\eta_1 = -1.96$
-5
-4
-3
-2
-1
0
1
2
3
4
5
η_2

Fig. 8c

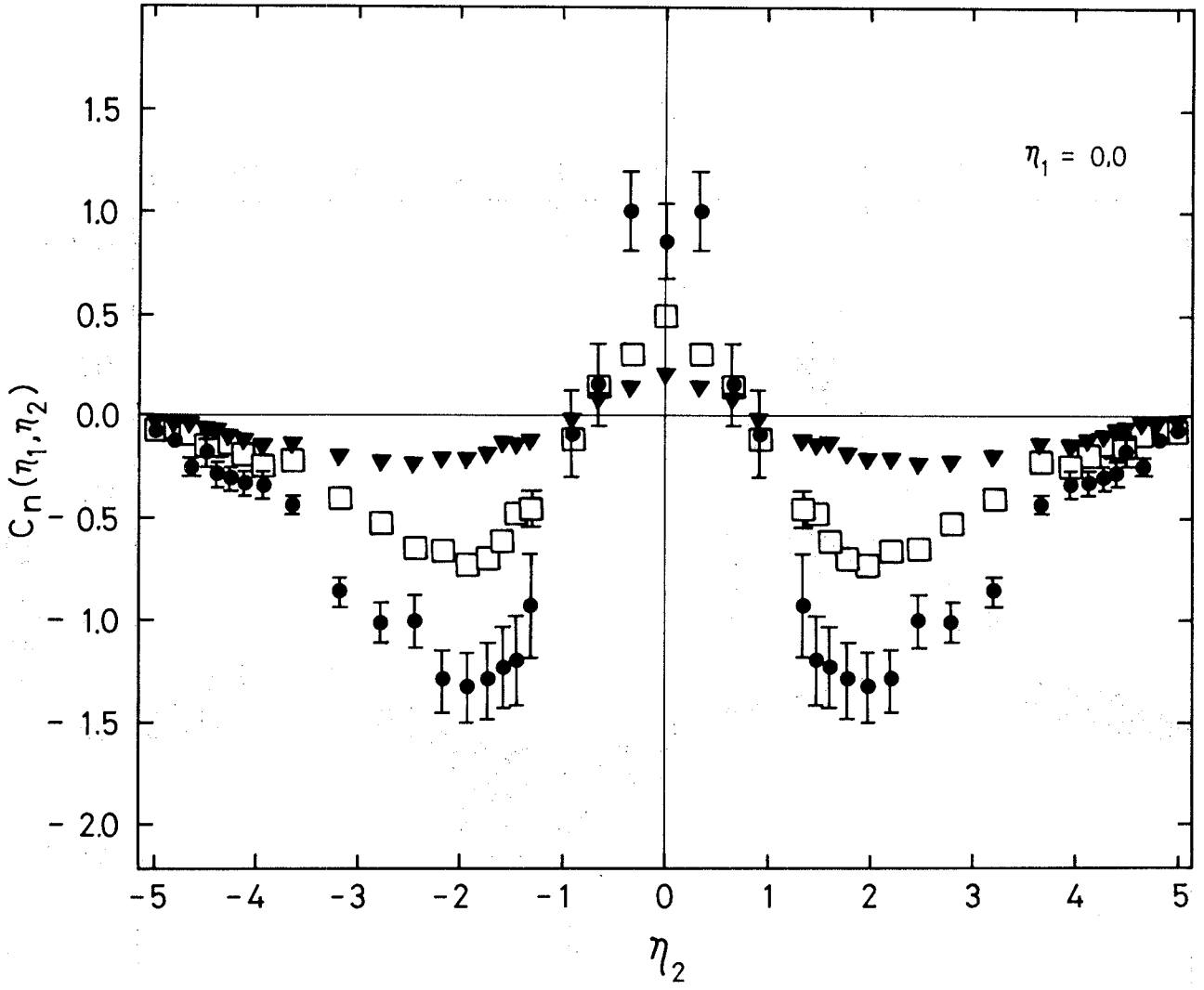

Fig. 9a

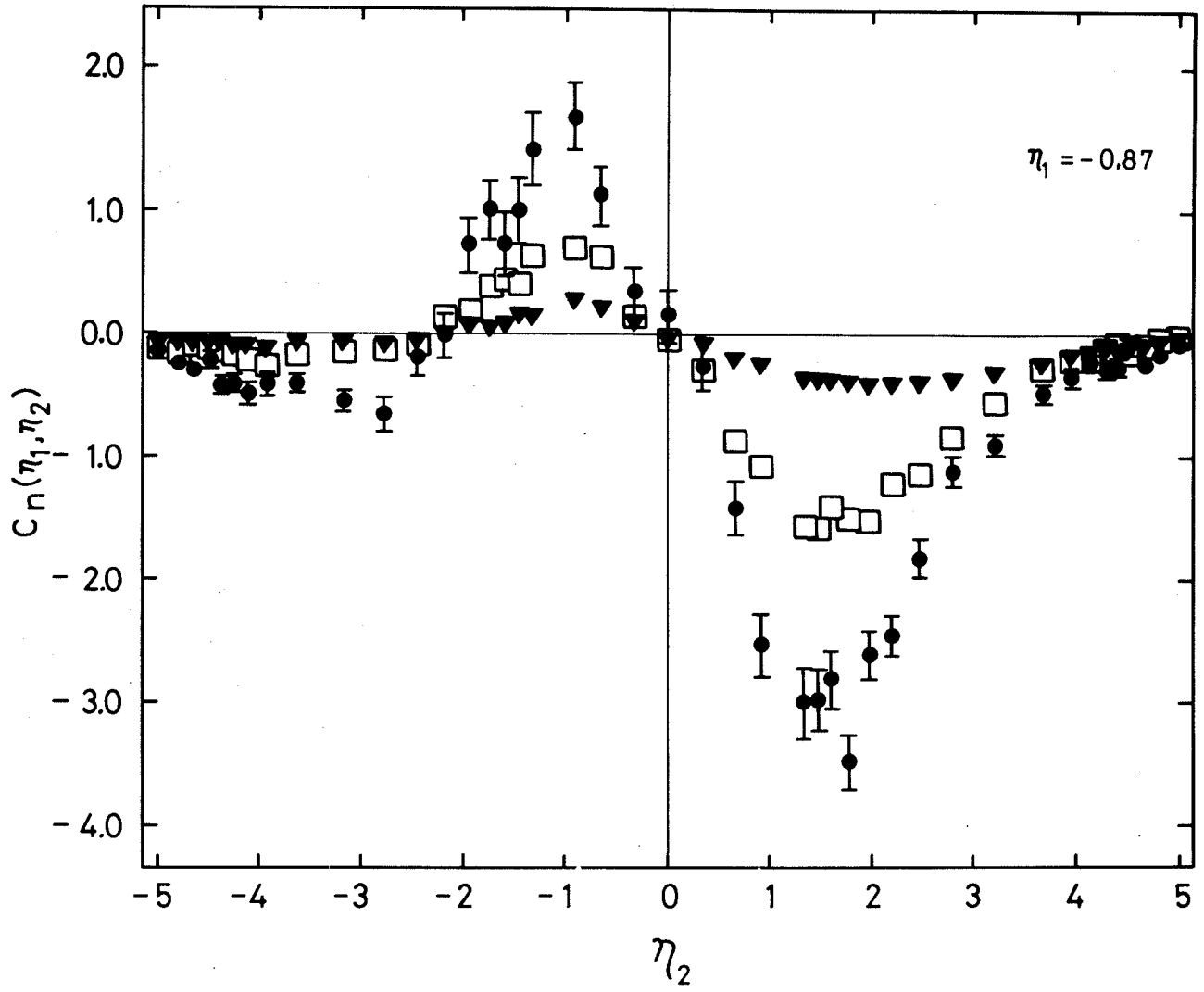

Fig. 9b

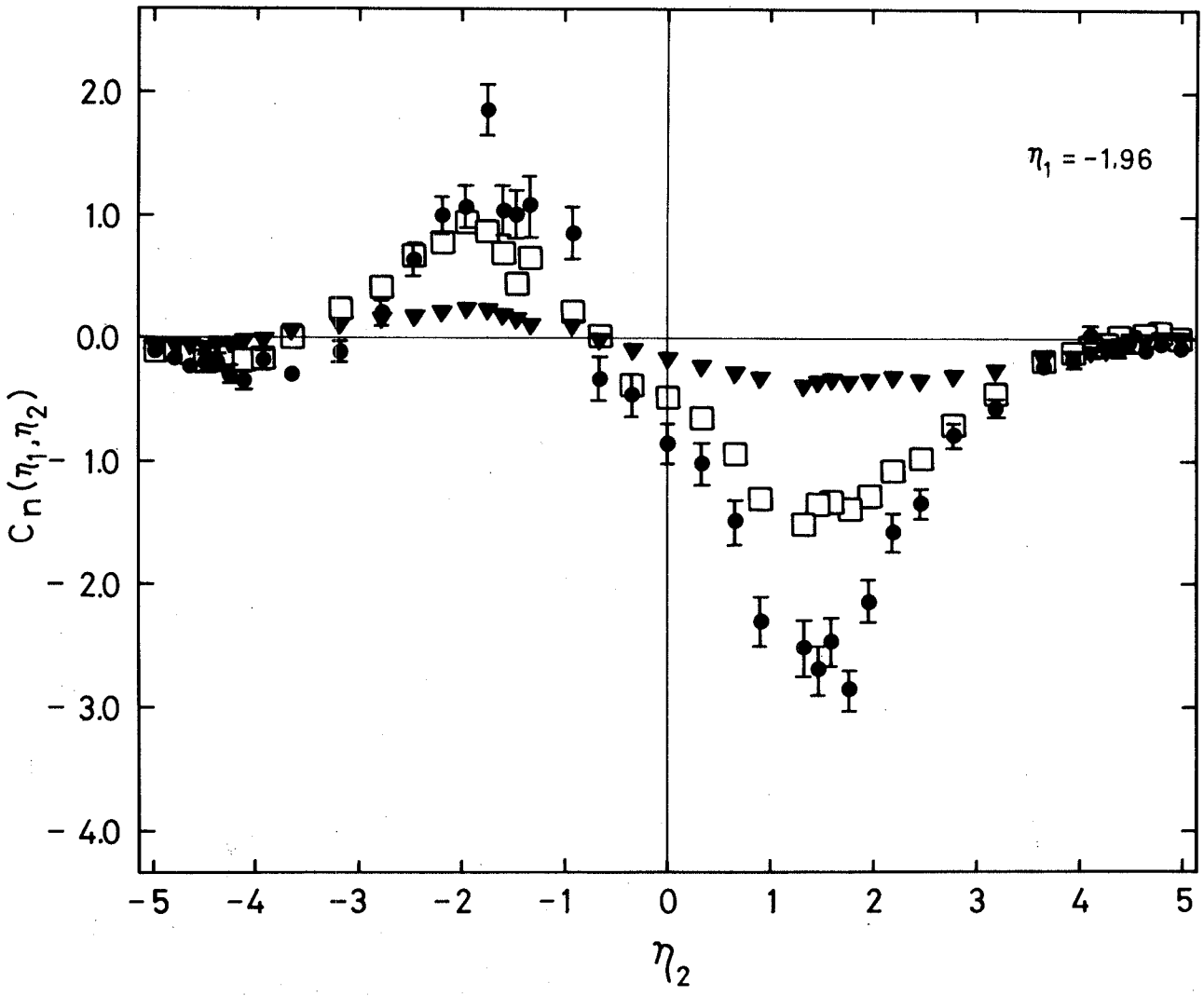

Fig. 9c

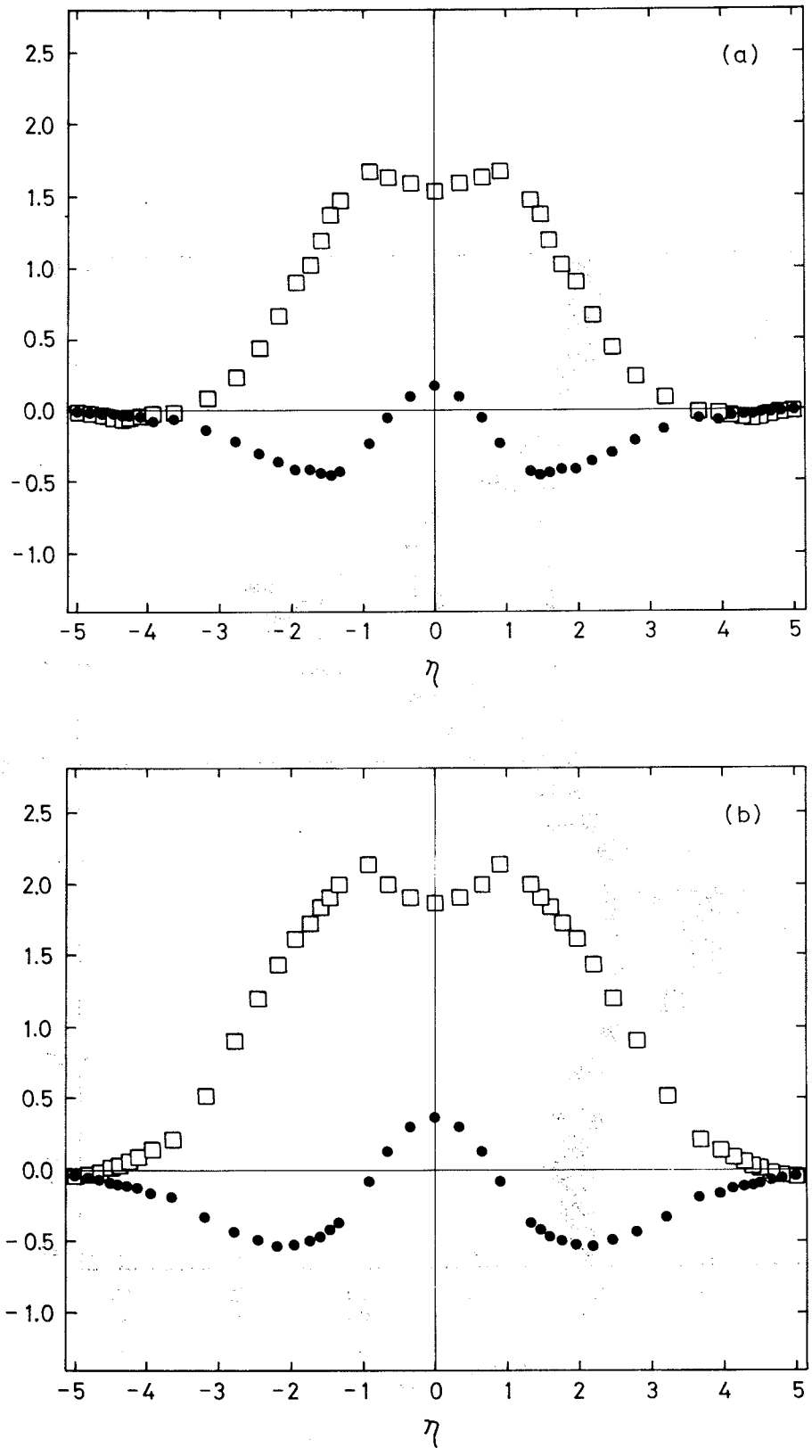

Fig. 10

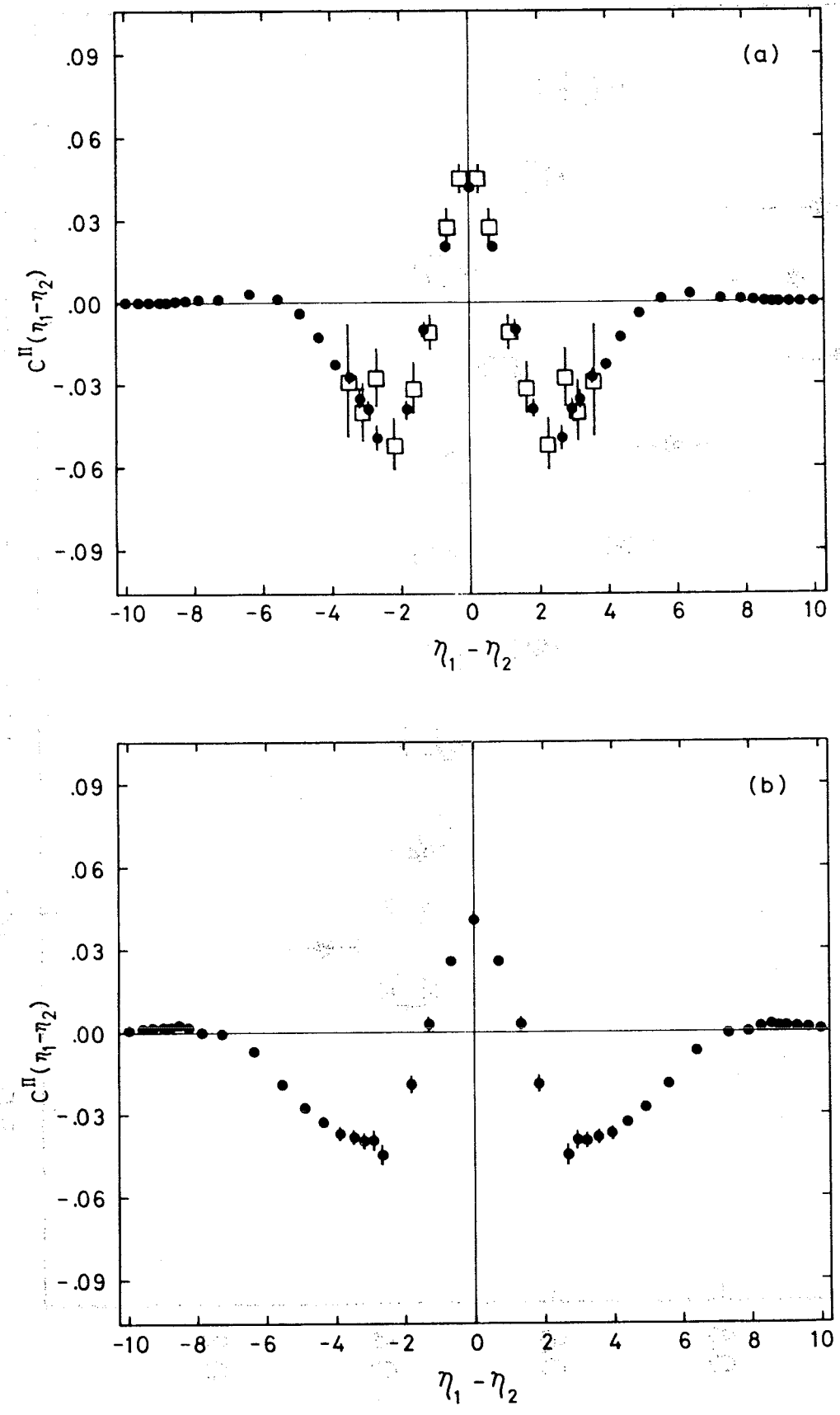

Fig. 11

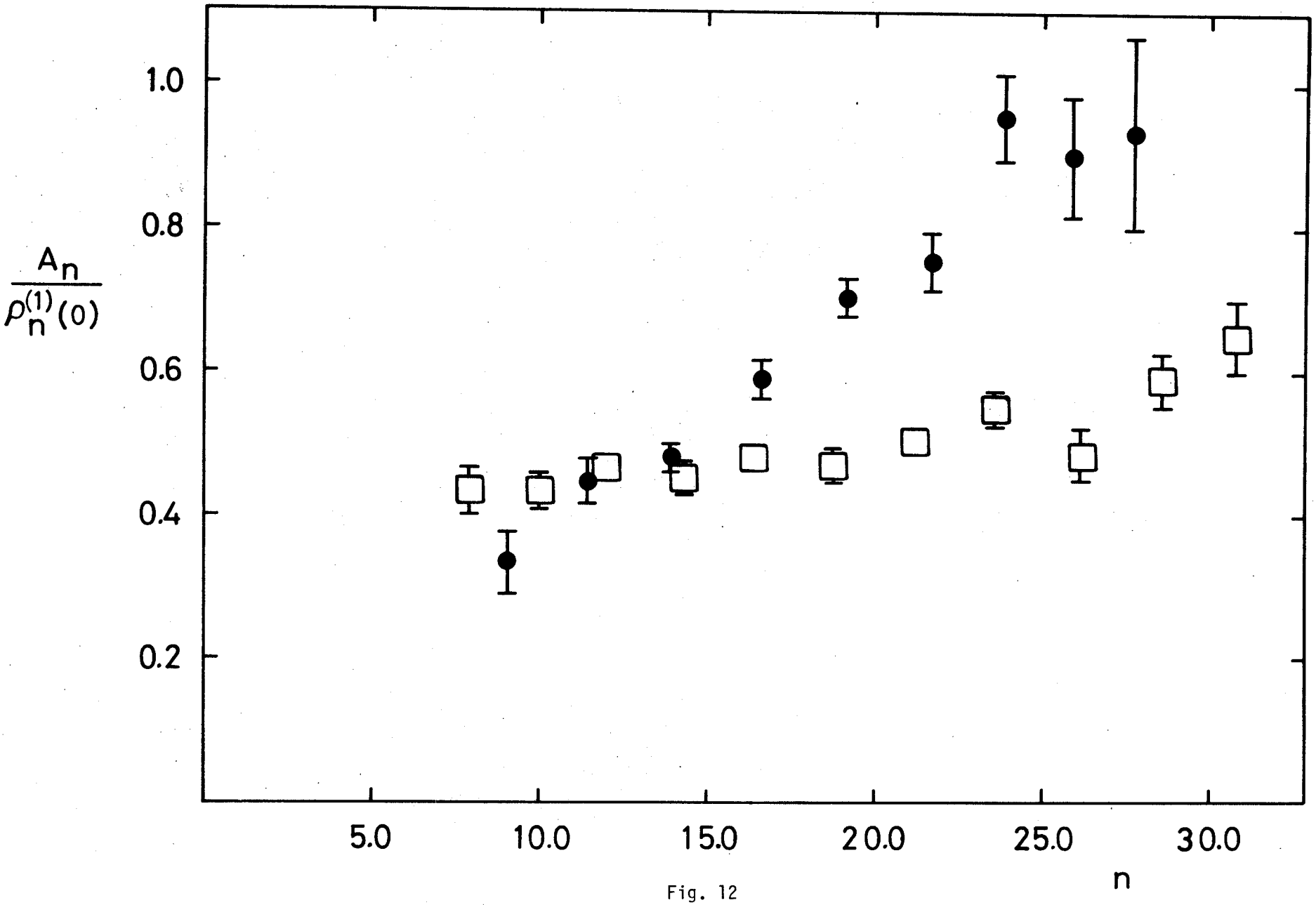

Fig. 12

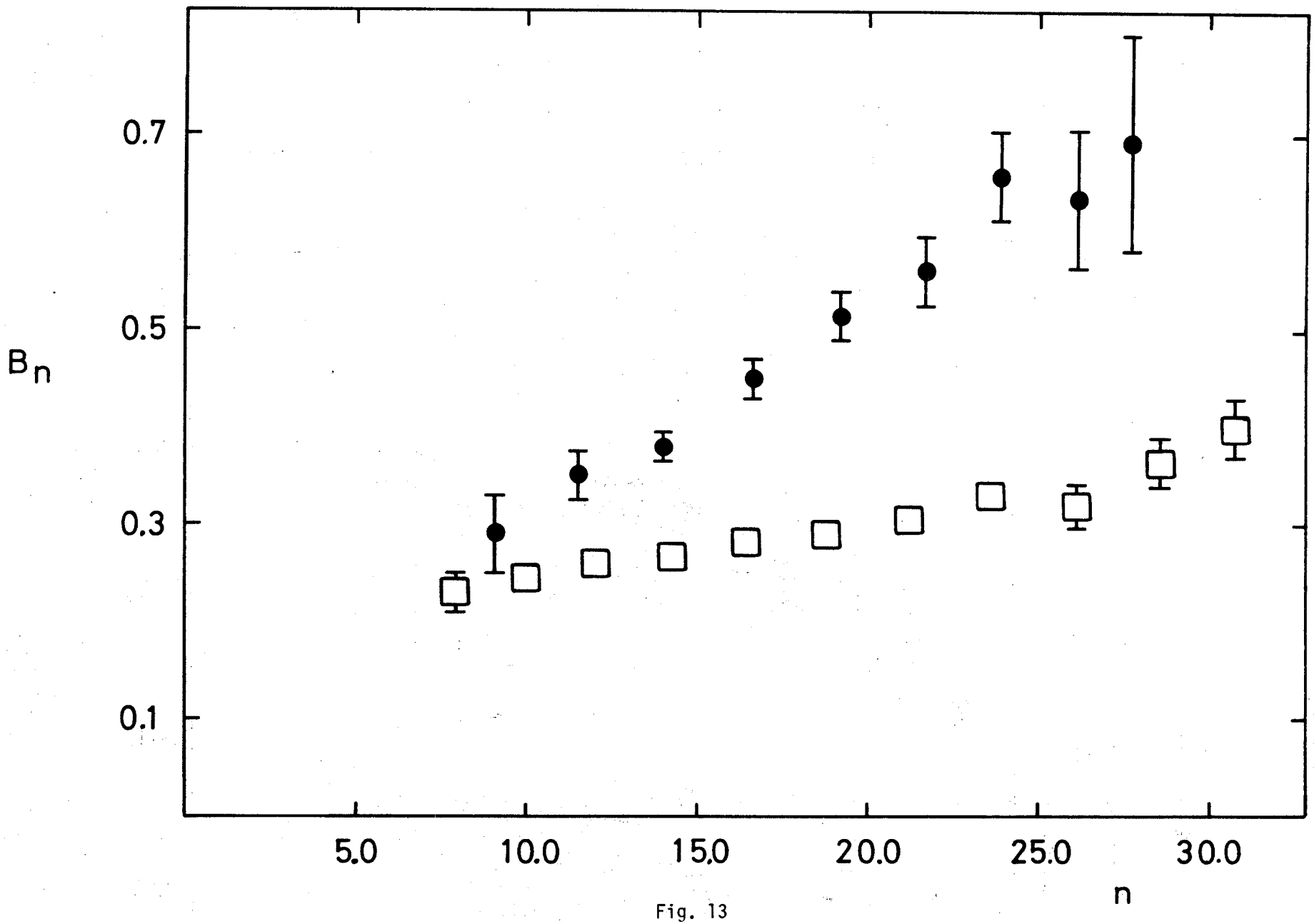

Fig. 13

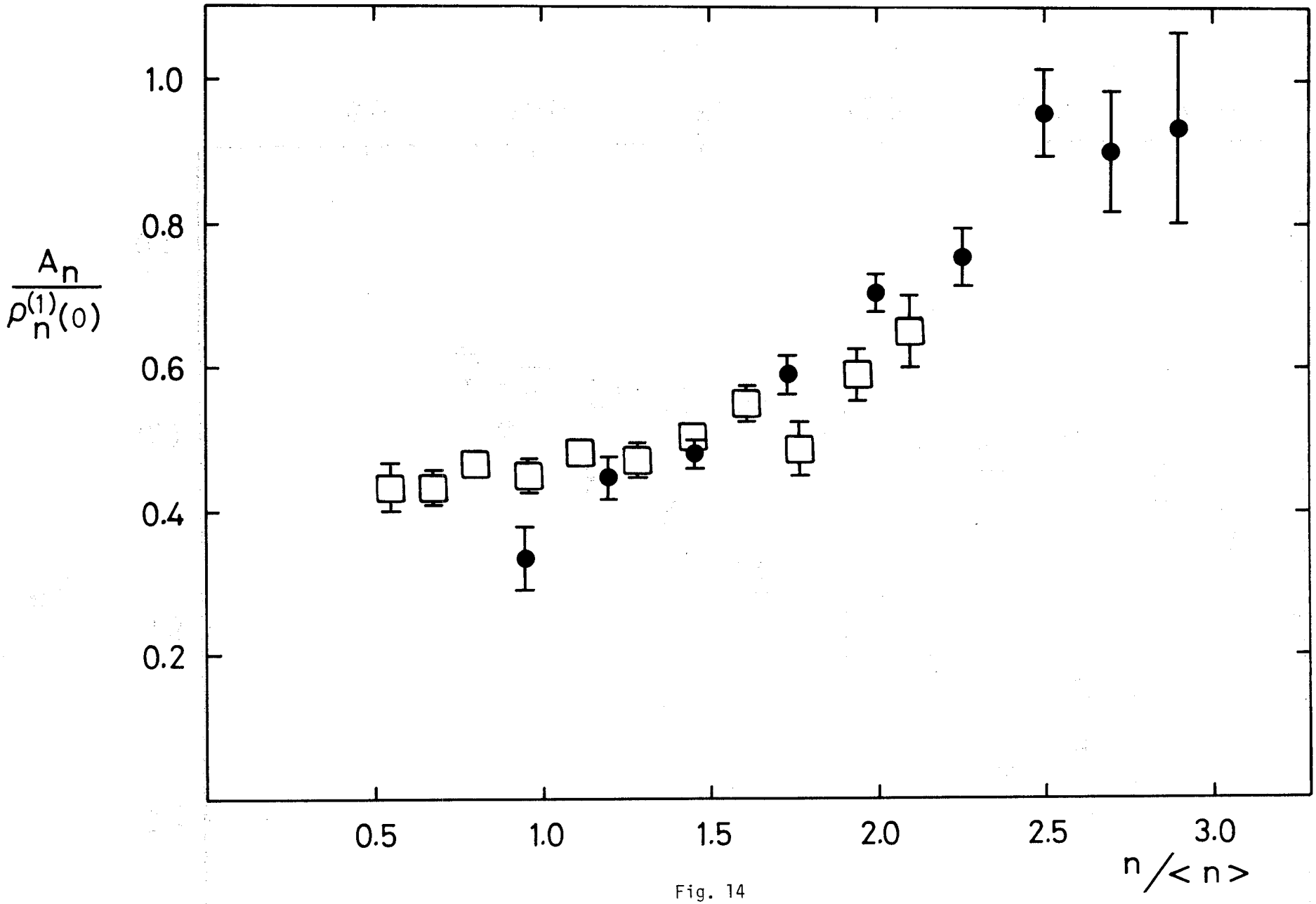

Fig. 14

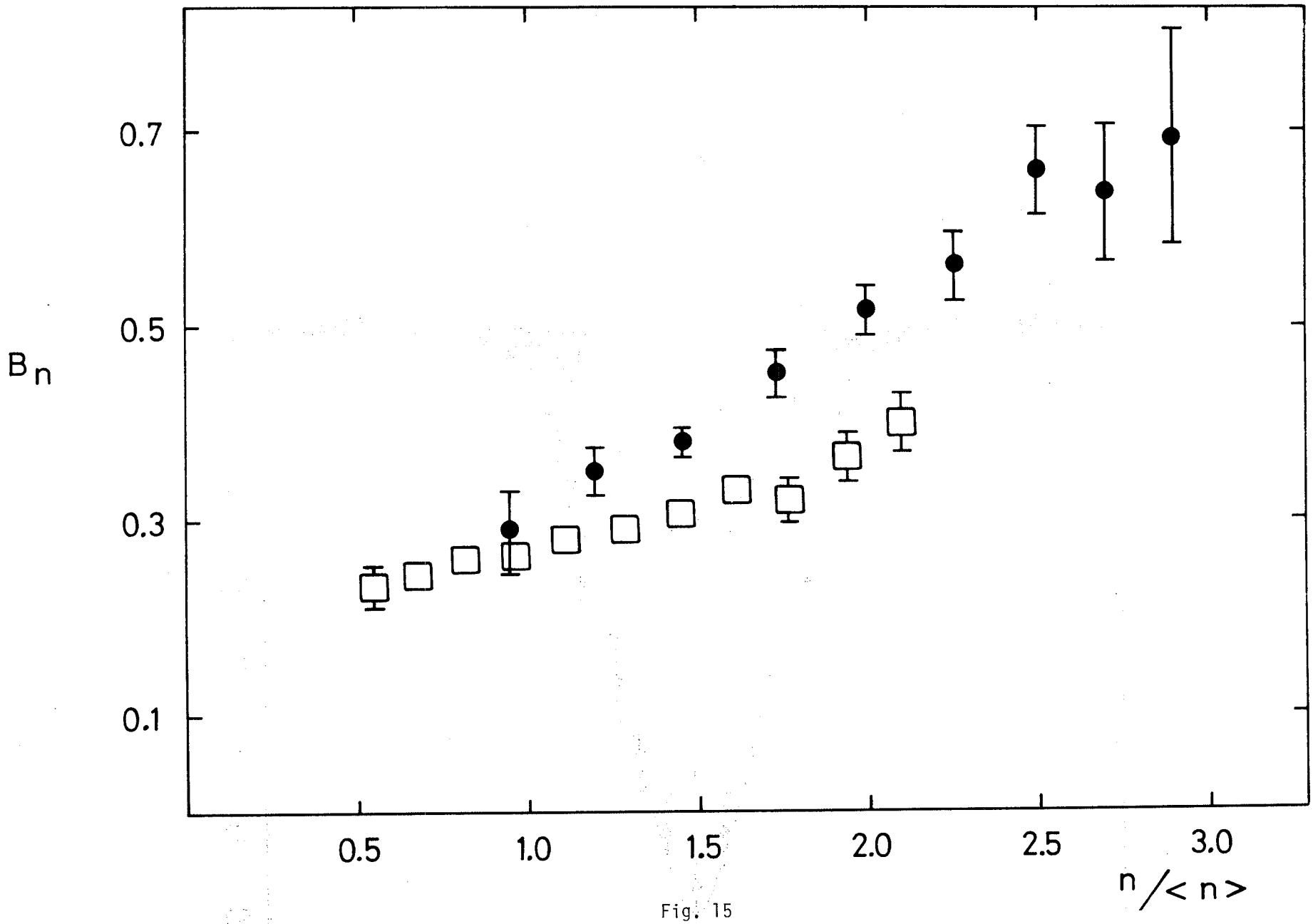

Fig. 15

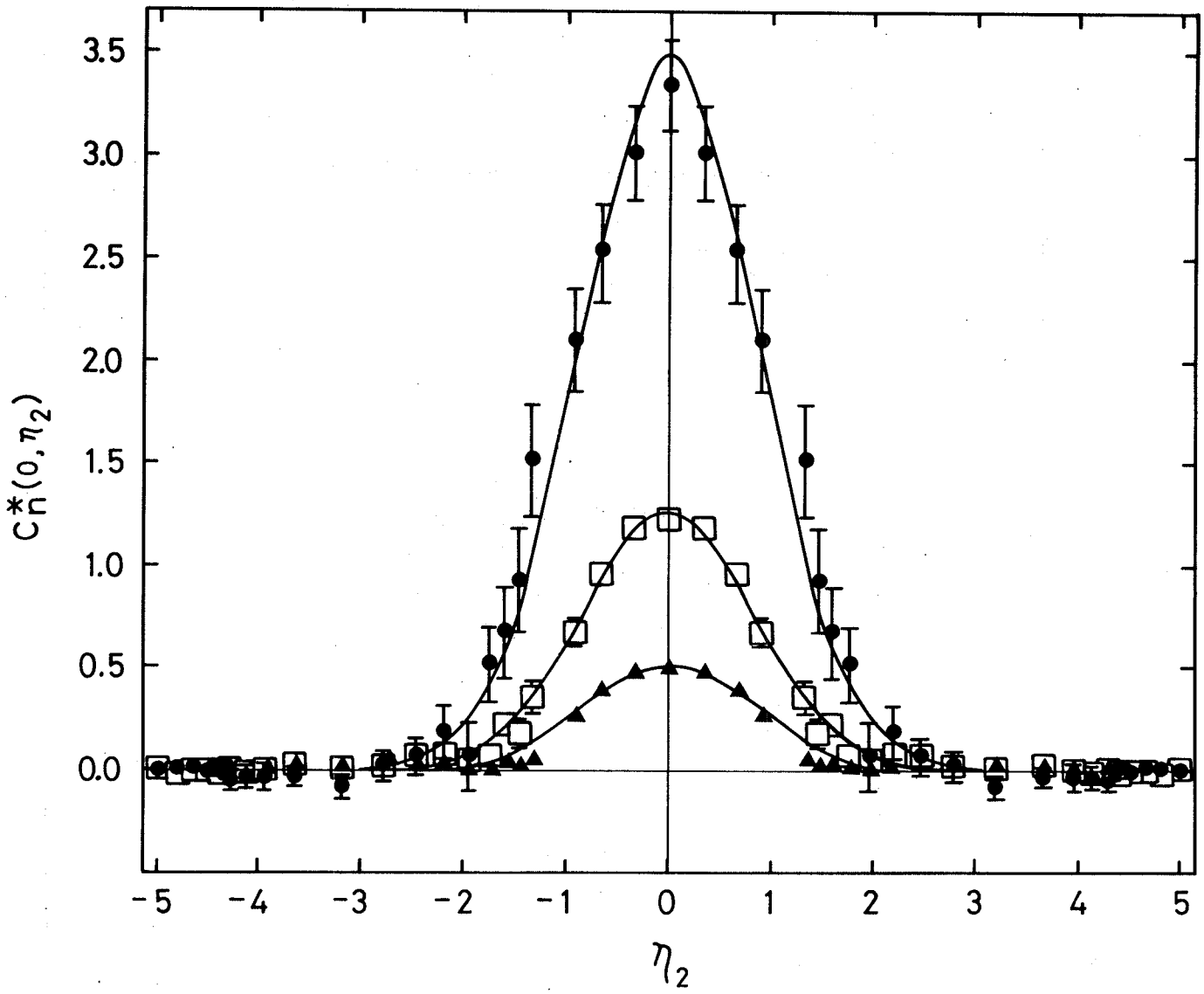

Fig. 16a

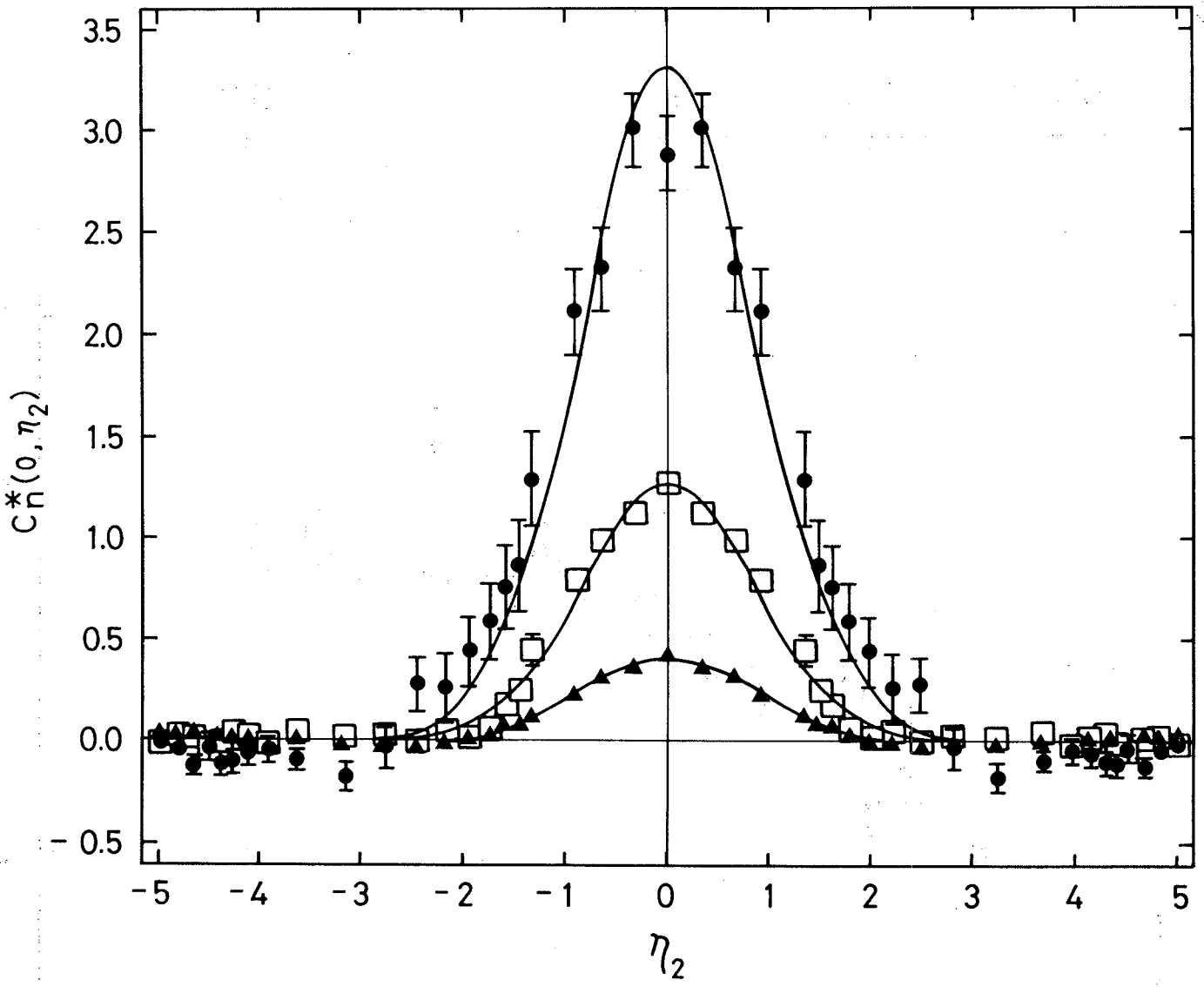

Fig. 16b

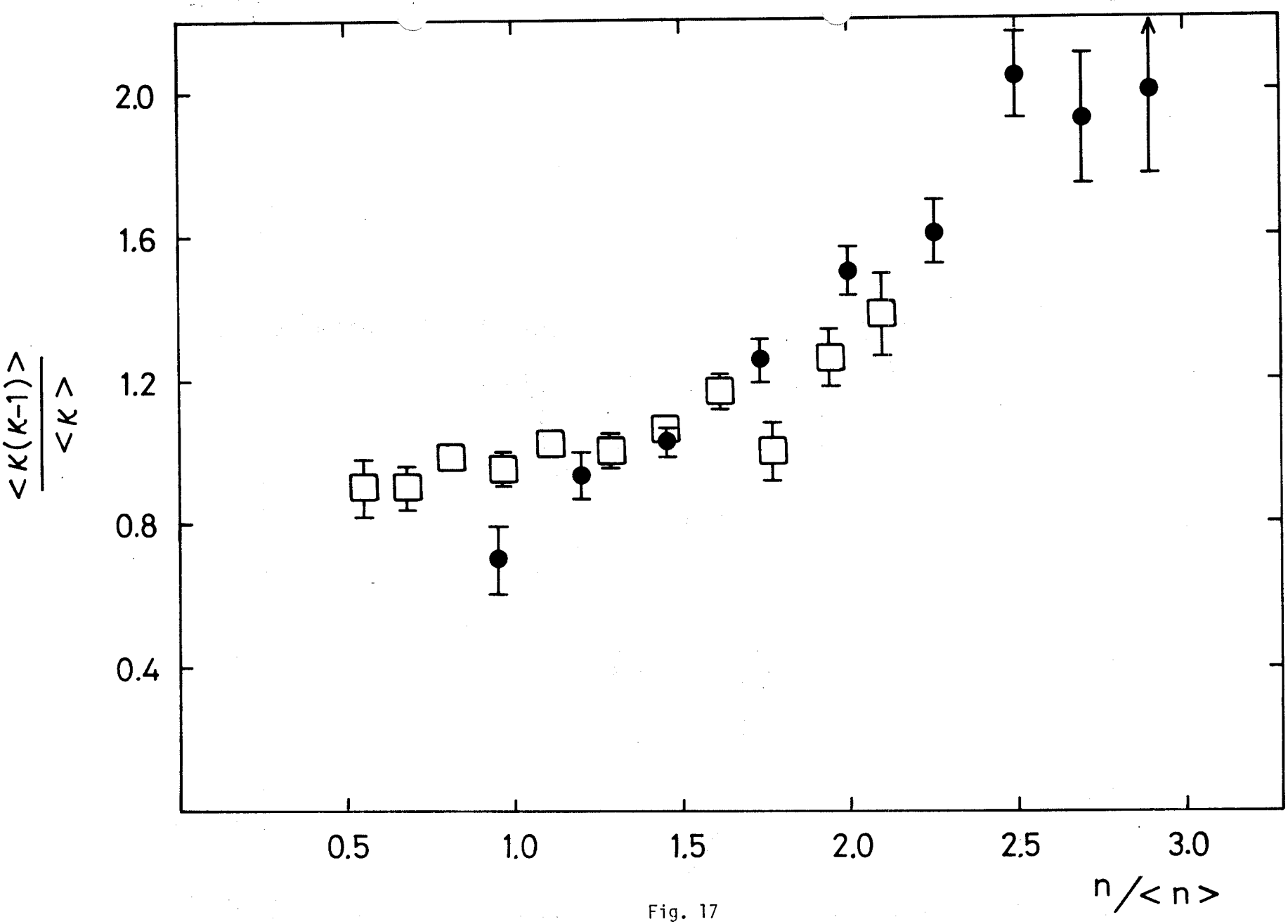
$\frac{\langle K(K-1)\rangle}{\langle K\rangle}$
2.0
1.6
1.2
0.8
0.4
0.5
1.0
1.5
2.0
2.5
3.0
$n/\langle n\rangle$

Fig. 17